

A ROBUST METHOD FOR ADDRESSING PUPIL DILATION IN IRIS RECOGNITION

By

Raghunandan Pasula

A THESIS

Submitted  
to Michigan State University  
in partial fulfillment of the requirements  
for the degree of

Computer Science – Master of Science

2016

## ABSTRACT

### A ROBUST METHOD FOR ADDRESSING PUPIL DILATION IN IRIS RECOGNITION

By

Raghunandan Pasula

The rich texture of the iris is being used as a biometric cue in several human recognition systems. Iris recognition systems are fairly robust to small changes in illumination and pose. However there are a number of factors that still adversely affect the performance of an iris matcher. These include occlusion, large deviation in gaze, low image resolution, long acquisition distance and *pupil dilation*. Large differences in pupil size increases the dissimilarity between iris images of the same eye.

In this work, the degradation of match scores due to pupil dilation is systematically studied using Hamming Distance histograms. A novel rule-based fusion technique based on the aforementioned study is proposed to alleviate the effect of pupil dilation. The proposed method computes a new distance score at every pixel location based on the similarities between IrisCode bits that were generated using Gabor Filters at different resolutions.

Experiments show that the proposed method increases the genuine accept rate from 76% to 90% at 0.0001% false accept rate when comparing images with large differences in pupil sizes in the WVU-PLR dataset. The proposed method is also shown to improve the performance of iris recognition on other non-ideal iris datasets. In summary, the use of multi-resolution Gabor Filters in conjunction with a rule-based integration of decisions at the pixel (bit) level is observed to improve the resilience of iris recognition to differences in pupil size.

## ACKNOWLEDGEMENTS

I would like to thank Dr. Arun Ross for his continued support and guidance through out my student career. No amount of thanks would be sufficient to describe the support extended by the family members by just being there for me and supporting me through the degree program.

Special thanks to Dr. Eric Torng and Katherine Trinklein for helping me through the tough times.

This work is dedicated to all the *gurus* who spend significant amount of effort and time to impart knowledge to the world.

## TABLE OF CONTENTS

LIST OF TABLES . . . . .	vi
LIST OF FIGURES . . . . .	vii
CHAPTER 1 INTRODUCTION . . . . .	1
1.1 Biometrics . . . . .	1
1.2 Eye anatomy . . . . .	4
1.2.1 Layers of eye . . . . .	5
1.2.2 Apparent iris texture . . . . .	9
1.2.3 Pupil dynamics . . . . .	12
1.3 Iris biometric system . . . . .	13
1.4 Challenges in Iris recognition . . . . .	20
1.5 Objectives of this work . . . . .	25
CHAPTER 2 MOTIVATION AND PREVIOUS WORK . . . . .	26
2.1 Motivation . . . . .	26
2.2 Previous work . . . . .	28
2.2.1 Minimum wear and tear model . . . . .	28
2.2.1.1 Wyatt 2000 . . . . .	28
2.2.1.2 Yuan and Shi 2005 . . . . .	31
2.2.1.3 Wei et al. 2007 . . . . .	32
2.2.2 3-D anatomical model . . . . .	33
2.2.2.1 Francois et al. 2007 . . . . .	33
2.2.2.2 Clark et al. 2012 . . . . .	34
2.2.3 Gejji et al. 2015 . . . . .	36
2.2.4 Other Deformation models . . . . .	36
2.3 Bit matching . . . . .	37
CHAPTER 3 COLLECTION OF DATABASE . . . . .	39
3.1 Motivation . . . . .	39
3.2 Data acquisition protocol . . . . .	39
3.3 Description . . . . .	40
3.4 Impact of pupil dilation . . . . .	42
CHAPTER 4 PROPOSED METHODS . . . . .	44
4.1 Multi-resolution Gabor filter encoding . . . . .	44
4.2 Typical IrisCode matcher . . . . .	45
4.3 Histogram of matching patterns . . . . .	46
4.4 Fusion . . . . .	48
4.4.1 Rule based Fusion . . . . .	49
4.4.2 Classifier based Fusion . . . . .	52
4.5 Experiments and Results . . . . .	52

4.6 Examples . . . . .	56
CHAPTER 5 SUMMARY . . . . .	60
5.1 Summary . . . . .	60
BIBLIOGRAPHY . . . . .	61

## LIST OF TABLES

Table 1.1	Wavelength range for visible, NIR and SWIR spectrum . . . . .	9
Table 3.1	Demographics distribution . . . . .	41
Table 3.2	Eye color information . . . . .	41
Table 4.1	Logical operations used to combine the output of multiple IrisCodes. . . . .	52

## LIST OF FIGURES

Figure 1.1	Figure showing the external anatomy of the human eye in the RGB spectrum. The focus of this thesis is on the iris, which is the annular textured structure situated between the pupil and the sclera. The iris is typically imaged in the near infrared (NIR) spectrum and not in the RGB spectrum. . . . .	2
Figure 1.2	A biometric system, during the, enrollment stage adds a template belonging to a new user into the Gallery. . . . .	3
Figure 1.3	Sagittarial cross-section of iris. Image published here with permission from [1]	6
Figure 1.4	Different layers of iris when looking into sagittal axis. . . . .	7
Figure 1.5	Location of sphincter and dilator muscles that control pupil constriction and dilation, respectively. . . . .	8
Figure 1.6	Path from light source to the eye . . . . .	10
Figure 1.7	Figure showing wavelengths of electro-magnetic spectrum relevant to iris biometrics . . . . .	11
Figure 1.8	Absorption spectrum of (a) liquid water [2] and (b) melanin [3] at different wavelengths of electromagnetic spectrum . . . . .	11
Figure 1.9	Example of blue, yellowish and dark brown iris images that contain low, moderate and high concentration of melanin, respectively. . . . .	12
Figure 1.10	Dark iris in (a) imaged at (b) 470nm, (c) 520nm, and (d) 700nm and (e) NIR wavelengths. . . . .	12
Figure 1.11	Examples of factors influencing the size of the pupil. . . . .	13
Figure 1.12	Components of a typical iris recognition system . . . . .	14
Figure 1.13	(a) Real part and (b) Imaginary part of a Gabor filter . . . . .	18
Figure 1.14	(a) Original acquired Image (b) Segmentation output (c) Normalized image (d) Corresponding mask image (e) IrisCode generated by encoding the normalized image using Masek's method. [4] . . . . .	19
Figure 1.15	Examples of non ideal iris images. (a) and (b) Non-uniform illumination, (c) and (d) Eyelid occlusion, (e) Eyelash occlusion, (f) Motion blur. . . . .	22
Figure 1.16	Examples of off-axis iris images. . . . .	22

Figure 1.17	Few examples of eye diseases that impact iris recognition (a) Polycoria - Multiple pupil openings (b) Coloboma - Tear in iris (c) Severe cataract - Thickening of lens (looses transparency). Although the images are shown in RGB, some of these diseases can also impact the NIR images. . . . .	24
Figure 2.1	(a) and (b) Iris image with moderate pupil size and the corresponding normalized iris image. (c) and(d) Iris image with large pupil size and the corresponding normalized iris image. Highlighted regions in (c) and (d) do not align correctly. Images from [5]. . . . .	27
Figure 2.2	Iris images with dilation ratios of (a) 0.3478 and (b) 0.6545. Images from [6]. . . . .	27
Figure 2.3	Iris mesh work proposed by Rohen [7]. Image from [7]. . . . .	29
Figure 2.4	$\theta_o$ is the angle between starting point of the fiber arc on pupillary boundary and ending point on limbic boundary. . . . .	30
Figure 2.5	Optimum arcs derived by Wyatt [8] for $\theta = 100^\circ$ , and pupil diameter 1.5, 4.0 and 7.0 mm . . . . .	30
Figure 2.6	Normalization model proposed by Yuan and Shi. Image from [9]. . . . .	31
Figure 3.1	Image sequence capture starts at $t_0 = 0$ . After approximately 10 seconds, at $t_1$ , the light source is turned on illuminating the eye for 10 more seconds $[t_1, t_2]$ . At $t_2$ the light source is turned off and remains off for 10 more seconds $[t_2, t_3]$ . The video capture is stopped at $t_3$ . . . . .	40
Figure 3.2	Sample images from the dataset . . . . .	41
Figure 3.3	Distribution of pupil dilation ratios in the dataset. They range from 0.2177 to 0.6367. . . . .	42
Figure 3.4	Distribution of genuine Hamming distance scores as a function of dilation differences. (a) $ D1 - D2 $ and (b) $ R1 - R2 $ . . . . .	43
Figure 4.1	A normalized image is encoded using multi-scale filters to result in an IrisCode set along with a mask showing valid bits in each IrisCode. This mask is same for all the codes in the IrisCode set . . . . .	45
Figure 4.2	A normalized image and its corresponding IrisCode generated using 3 filters. These filters encode the image at multiple scales. . . . .	45
Figure 4.3	A typical iris matcher. Match scores are computed independently at each scale which are then fused at score level to result in a final distance score. . . . .	47

Figure 4.4	Distribution of multi-filter decisions for genuine matching cases for a single subject. . . . .	48
Figure 4.5	Distribution of multi-filter decisions for randomly selected impostor matching cases . . . . .	49
Figure 4.6	Comparison of distributions of possible multi-filter decisions for genuine and impostor matching cases . . . . .	50
Figure 4.7	The proposed iris matcher sequentially combines the results at multiple scales and generates a single decision result. . . . .	51
Figure 4.8	Flowchart depicting Method 1 and its corresponding truth table . . . . .	53
Figure 4.9	Flowchart depicting Method 2 and its corresponding truth table . . . . .	54
Figure 4.10	Flowchart depicting Method 3 and its corresponding truth table . . . . .	55
Figure 4.11	(a) ROCs for full data. The genuine and impostor score distributions are plotted for (b) Method 1, (c) Method 2 and (d) Method 3. . . . .	56
Figure 4.12	ROCs generated by using the genuine scores for pairs whose pupil dilation ratio differences are (a) small, (b) medium and (c) large. The impostor distributions are held the same across all the cases. . . . .	57
Figure 4.13	The histogram of genuine and impostor scores using Masek’s method and after fusion of match scores from Masek’s method and proposed Method 1. . . . .	58
Figure 4.14	ROC curves for (a) WVU and (b) QFire datasets. The improvement in GAR is clearly evident at low FARs. . . . .	58
Figure 4.15	Genuine pairs of images that were correctly matched using the proposed method but were incorrectly rejected by the traditional matching method at 0.0001% FAR. . . . .	59

# CHAPTER 1

## INTRODUCTION

*“To suppose that the eye with all its inimitable contrivances for adjusting the focus to different distances, for admitting different amounts of light, and for the correction of spherical and chromatic aberration, could have been formed by natural selection, seems, I confess, absurd in the highest degree.”*

— Charles Darwin, *On the Origin of Species*

Eye is an extremely complex and yet balanced organ in the human body. Human eye is a nearly spherical organ whose primary function is to allow for human *vision*. The visible part of the eye appears as shown in Figure 1.1 [10]. It is comparable to an optical system that captures the imagery of a scene and projects it on to a sensor known as retina in the back of the eye.

Textural pattern of human iris (see Figure 1.1) is believed to be unique to each individual. This is exploited in the field of biometrics to recognize individuals.

### 1.1 Biometrics

Passwords and keys have been the cornerstone of authentication. However, biometrics has made inroads into the world of secure authentication and surveillance in the 21<sup>st</sup> century [11]. ISO/IEC 2382-37:2012 [12] defines *biometrics* as the science of automatically recognizing individuals based on their biological and behavioral characteristics. Examples include recognizing humans based on their fingerprint, face, iris and hand geometry among others. Unlike passwords that have to be remembered or keys/tokens that have to be physically carried, biometrics are intrinsically associated with the users themselves. A large study of web password habits by Microsoft [13] on half million users found that an average user has 6.5 passwords and uses them across an average of 25 accounts. It gets increasingly harder to create and remember new passwords. Secure access to physical locations typically requires keys or tokens such as magnetic cards. Most locations also

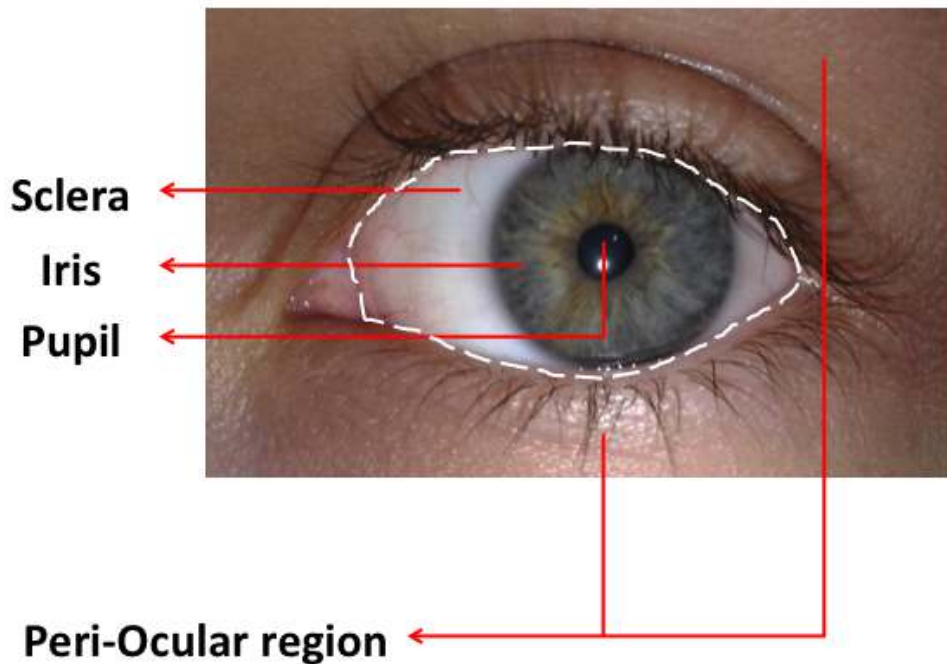


Figure 1.1 Figure showing the external anatomy of the human eye in the RGB spectrum. The focus of this thesis is on the iris, which is the annular textured structure situated between the pupil and the sclera. The iris is typically imaged in the near infrared (NIR) spectrum and not in the RGB spectrum.

require the user to type in a password besides producing a token or a key. The users cannot be authenticated in case the user forgets the password or forgets to bring the keys/tokens. Biometrics eliminates these stringent requirements and only needs the user to interact with the system. A good biometric trait [14] is universal - all users have it, permanent - it is stable through the lifetime of a user, distinct - it is unique across multiple users and is easily collectible. Biometrics has been successfully deployed in real world applications including surveillance, immigrant verification at the port of entry, access control, ATMs and even identifying lost children.

A classical biometric system consists of a biometric sensor (typically a camera imaging the

biological trait), a feature extractor, a matcher and a database module (see Figure 1.2). A biometric sensor captures the biometric data from the user, generally in the form of a digital signal. The captured signal may have to be pre-processed to identify the region of interest or enhanced to improve its quality. Then a feature extractor transforms the data into a numerical pattern that can later be used for comparison.

A biometric system in practice is operated in one of the following three modes.

### Enrollment

In this mode, a user is enrolled by adding his/her features to a database known as *gallery*. Features *stored* in the database from the acquired digital signal are referred to as a *template* during enrollment. In a cooperative environment, an identity in the form of a label is assigned to each stored template. It is also possible to have a system where the identity of an enrolled template is unknown and labeled using nominal identifiers [15].

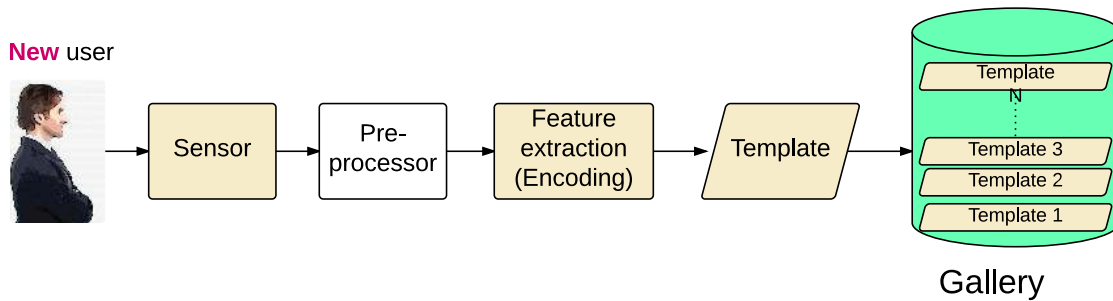


Figure 1.2 A biometric system, during the, enrollment stage adds a template belonging to a new user into the Gallery.

### Verification

In the verification mode, the user interacting with the system claims an identity. For example, consider a biometric system deployed to recognize a person entering the United States. Bob, who is already enrolled into the Gallery, is now interacting with the system claiming that he

is Bob and would like to enter the country. The sensor collects the biometric data (*probe*) and extracts a feature set. In verification mode a single gallery template corresponding to the claimed identity, in this case Bob, is retrieved from the gallery and *matched* against the probe feature set. If the similarity is greater than a threshold value, then the identity is successfully *verified*. Since the matching is performed between one probe and one gallery template, it is also referred to as 1:1 matching. This operational mode is typically used to grant access to secure facilities, verifying identity at the port of entry, etc.

## **Identification**

As in the case of verification, the feature set is extracted from the data acquired from a user. In this mode, the obtained feature set is matched against *all* the templates in the gallery in order to retrieve identities whose templates have similarity greater than a certain threshold. Since the matching is performed between one probe and all gallery templates, it is sometimes referred to as 1:N matching (N being the number of templates in the gallery). For example, Tom who is applying to enter a certain country may be required to present his biometric sample (fingerprint). The extracted feature set is then matched against a specific gallery containing templates of known criminals in order to find a possible match. Similarly, the identification mode can be used in surveillance scenarios to determine the identity of people at a particular location.

An iris recognition system has multiple components that are described in Section 1.3. In spite of the relatively high accuracy of iris recognition systems, they are highly susceptible to a variety of problems. For example, an acquired image that is out of focus may probably not be matched with its correct identity. This increases the False Rejection Rate (FRR) or the False Match Rate (FMR) [16]. Section 1.4 details current challenges in the field of iris recognition.

## **1.2 Eye anatomy**

The ocular region in Figure 1.1 is the anterior portion of the eyeball that is externally visible. The horizontal cross-section of the anterior ocular region broadly consists of three regions namely pupil, iris and sclera. Pupil is the dark hole in the center of the eye and sclera is the whitish portion of the eye. Iris is the textured and colored part of the eye enclosed between the pupil and sclera. The human visual system is comparable to an optical camera system where the pupil may be considered as the lens/aperture and the iris as the aperture stop that controls the size of the aperture.

In the context of biometrics, the ocular traits traditionally refer to physical or behavioral attributes in the eye globe such as iris [17], conjunctival vasculature in episclera [18], retinal vasculature [19], Oculomotor Plant Characteristics (OPC) [20] and Complex Eye Movements (CEM) [21]. Periocular region [22] consists of upper and lower eyelids, and a fixed rectangular region around the eye. The upper eyelid is a type of skin fold that is able to stretch out and cover the eye to protect it from dust, debris and sunlight. Periocular region may also contain other identifiable features such as eye brows and moles on the skin in the vicinity of the eye region.

### **1.2.1 Layers of eye**

Since the iris texture is treated as a biometric trait, it is important to understand its structure, components, physiology and spectral properties. Since the eye is a 3 dimensional object, the image of an eye is merely a 2 dimensional representation of the original shape. Figure 1.3 shows the sagittal cross-section of an eye.

From an image acquisition perspective, the light from the source encounters cornea, aqueous humor, iris and lens after which it is projected on to the retina.

#### **Cornea**

Light from an object enters the eye through the cornea which is a transparent protective tissue layer protecting the eye from external world. It is the first defensive system employed

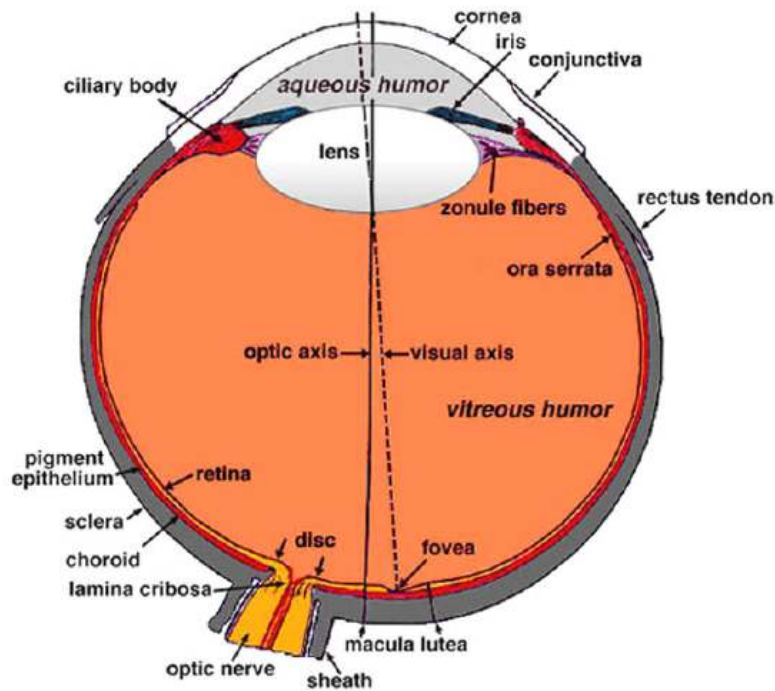


Figure 1.3 Sagittarial cross-section of iris. Image published here with permission from [1]

by the eye. It covers the entirety of iris with an approximate diameter of  $11.8\text{mm}$ . The refractive index of corneal layer is approximately 1.33. The light undergoes refraction since it is passing from air with a refractive index of 1.0 to corneal layer with a refractive index of 1.33. Hence, it acts as a focusing element that focuses the incoming light into the pupil.

### **Aqueous humor**

Once the light crosses cornea, it enters a watery medium known as aqueous humor. This region is also referred to as the anterior chamber of the iris. Aqueous humor inflates the ocular region and helps in maintaining ocular pressure while transporting required nutrients to iris tissues. Aqueous humor consists of 98% water and small portions of amino acids, electrolytes, ascorbic acid, glutathione and immunoglobulins. Spectral properties of aqueous humour may be approximated to that of water since it is 98% water and is usually transparent in the visible and near-infrared spectrum.

## Iris

After the light passes through aqueous humor, it encounters the annular iris region with a hole in the center. The iris acts as a diaphragm between the anterior and posterior chamber of the eye. The iris is primarily divided into three layers - stroma, sphincter and dilator muscles, and pigmented epithelium. These components are pictorially shown in Figure 1.4.

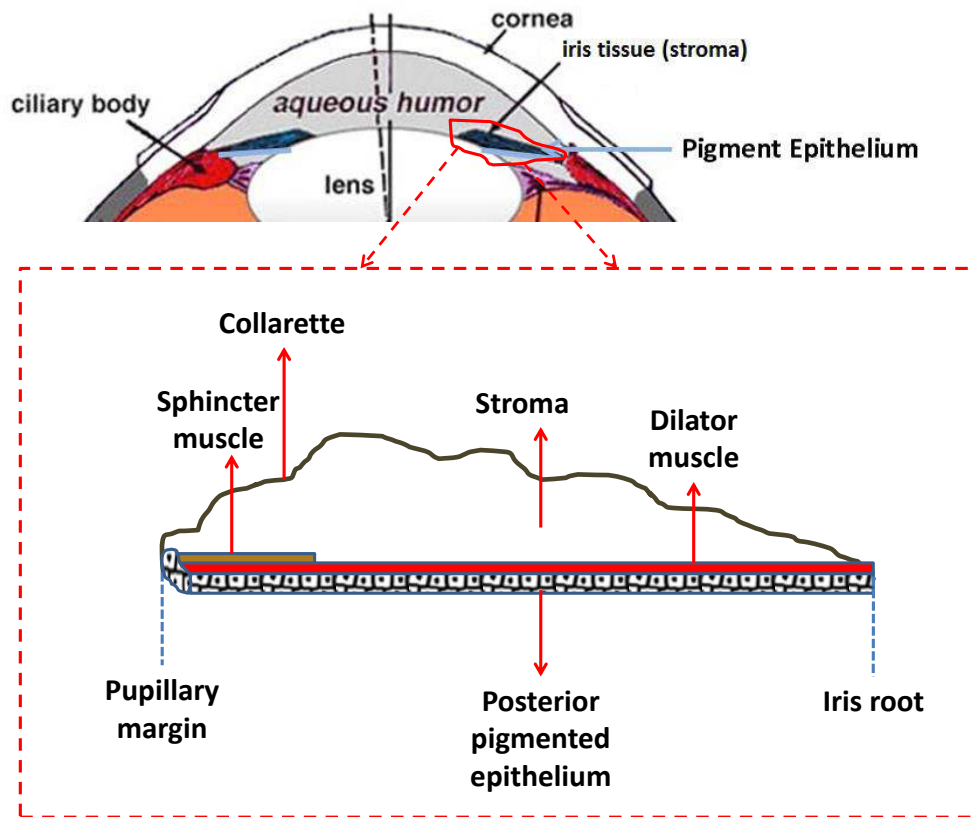


Figure 1.4 Different layers of iris when looking into sagittal axis.

The iris gains its texture from its elements in the anterior portion, i.e, stromal faetures such as fibrous tissues, crypts, anti-crypts, freckles, moles and concentration of a pigmentation material called melanin. The color of the iris is mostly impacted by the concentration of melanin in the stroma. Very low concentrations of melanin gives iris a bluish color, medium concentration gives it a green/yellow/hazel color and a high concentration of melanin gives

iris a very dark brown color. However, the incident and image acquisition wavelength also play a major role in the *apparent* texture of the iris.

Iris consists of a base layer of heavily pigmented cells known as *posterior pigmented epithelium*. Dilator muscle lines the top of this pigmented epithelium and is responsible for pupil dilation. Dilator muscles are radial and extend from iris root to pupillary ruff. Their contraction results in pulling the pupillary margin towards the iris root thereby *dilating* the pupil size. Sphincter muscle, on the other hand, is a circular (parallel to pupillary margin or concentric to pupillary boundary) muscle that extends from pupillary margin to an imaginary boundary known as *Collarette*. It can be observed from Figure 1.5 that the collarette is the boundary where sphincter and dilator muscles start to overlap. However it is important to note that both sphincter and dilator muscles are located beneath the stroma and hence are not visible to the naked eye.

### **Lens (pupil)**

Lens is a near transparent crystalline biconvex structure that is located behind the iris and supported by suspensory ligament which is in turn connected to the ciliary body. Part of the lens not covered by the iris is visualized as a dark hole known as pupil in the eye image, since all the light entering the lens is finally absorbed by the vitreous humor behind the lens. The lens along with the cornea accounts for all the focusing power of the eye's optical system and helps to focus the incoming light onto the retinal wall on the back of the eye. The light intensity on retina is converted into impulses which are then transmitted to the brain through the optical nerve. The extent of lens exposed to the light is controlled by sphincter and dilator muscles in iris.

### **1.2.2 Apparent iris texture**

As mentioned earlier, the apparent iris texture is dependent on the wavelength at which the iris image is acquired. Let us assume that there is sufficient illumination incident on the eye. Figure

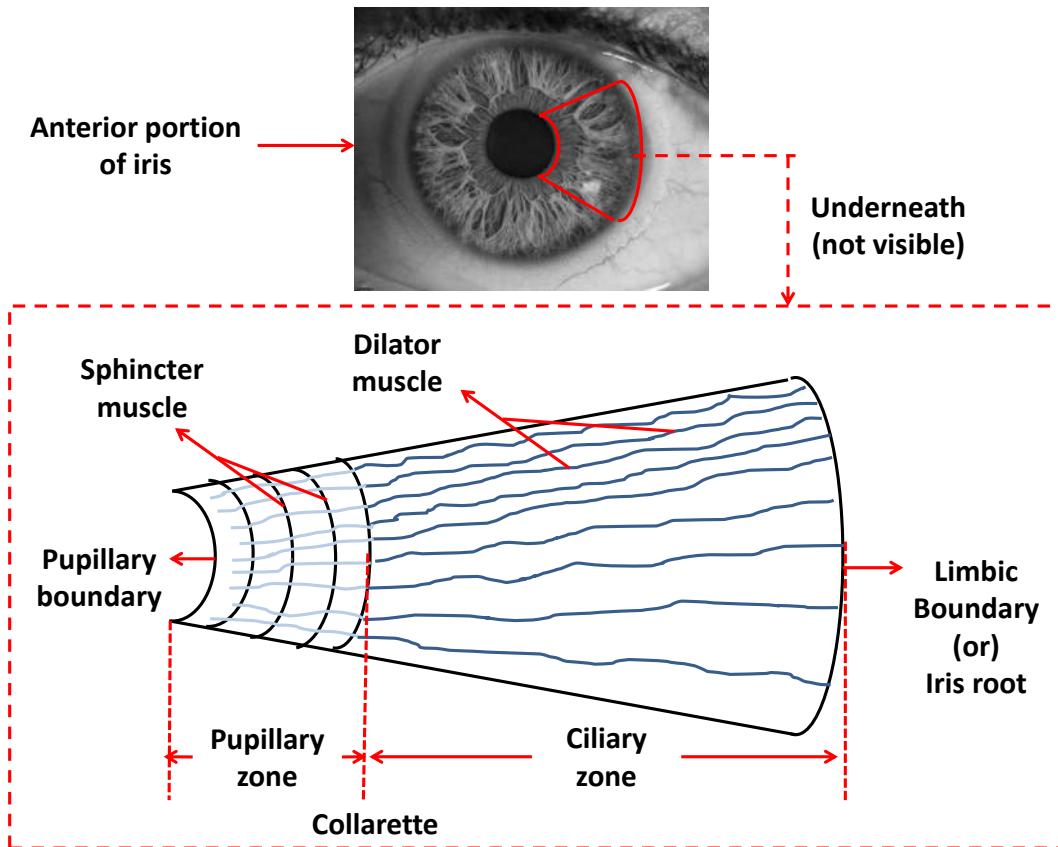


Figure 1.5 Location of sphincter and dilator muscles that control pupil constriction and dilation, respectively.

1.6 shows the major absorption elements on the path from the image acquisition camera to the eye. Since the base of iris is opaque and all the light is absorbed through the lens in the center, only the texture pertaining to anterior portion of iris is captured by the camera.

Table 1.1 and Figure 1.7 show the wavelengths of the electromagnetic spectrum that we are interested in and their corresponding names. Visible spectrum ranges from 450nm wavelength denoting bluish color to 700nm wavelength denoting reddish colors. Near Infra-Red (NIR) covers wavelengths from 700nm to 900nm and is usually considered monochromatic. Short Wave Infra-Red (SWIR) encompasses wavelengths from 900nm to 1600nm.

Absorption of liquid water and melanin are shown in Figure 1.8 (a) and (b). In visible spectrum, air and aqueous humor act as pass-through filters, while the light is scattered and reflected from tissues and melanin pigment in iris. Blue colored irises contain very minute concentrations of

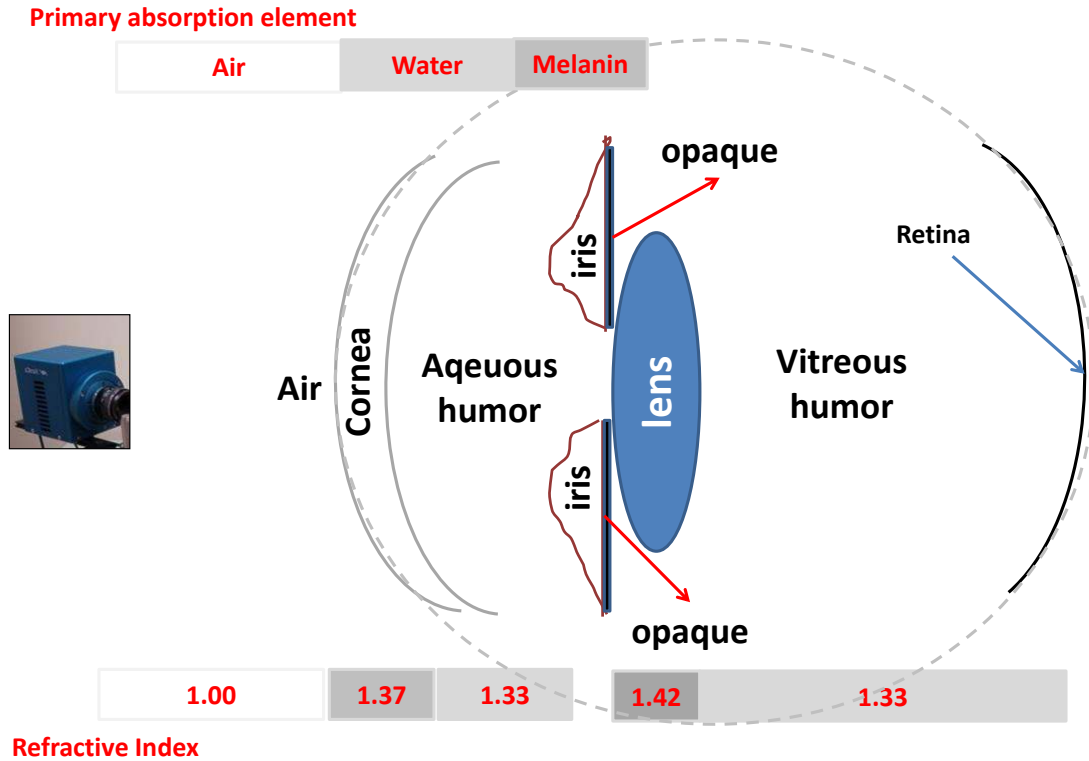


Figure 1.6 Path from light source to the eye

Table 1.1 Wavelength range for visible, NIR and SWIR spectrum

Spectrum	Wavelength range
Visible	400nm - 700nm
Near Infra-Red	700nm - 900nm
Short Wave Infra-Red	900nm - 1600nm

melanin, and, hence most of the incident light is scattered and internally reflected resulting in a bluish appearance (due to Tyndall effect [23]). Irises with high concentration of melanin appear dark brown in visible spectrum since melanin absorbs most of the incident illumination. Figure 1.9 shows examples of three iris images with varying levels of melanin content.

In NIR spectrum, the air and aqueous humor still act as pass-through filters while the absorption coefficient of melanin drops significantly after 700nm. This results in dark irises exhibiting good textural patterns revealing the meshwork of fibres, crypts and possible pigmentation spots. Figure 1.10 shows an image of a dark brown iris in visible spectrum exhibiting discernible textural patterns

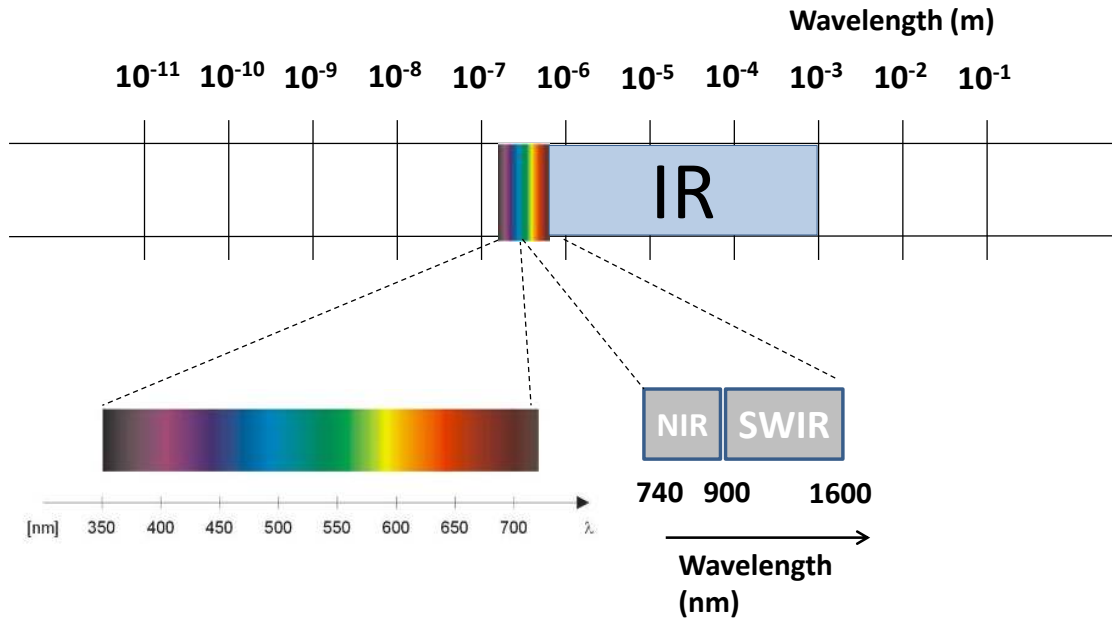


Figure 1.7 Figure showing wavelengths of electro-magnetic spectrum relevant to iris biometrics

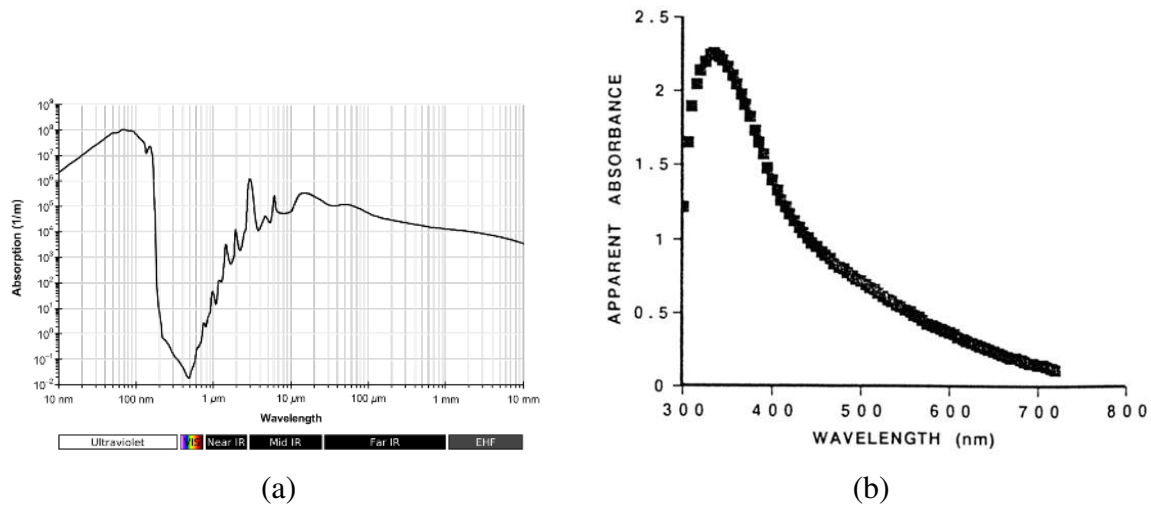


Figure 1.8 Absorption spectrum of (a) liquid water [2] and (b) melanin [3] at different wavelengths of electromagnetic spectrum

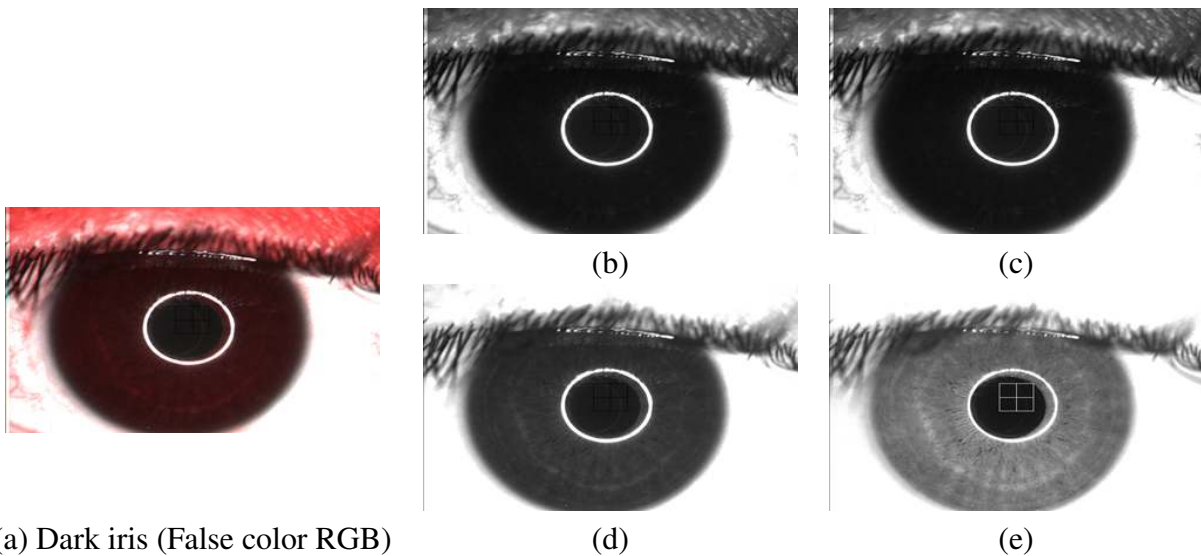
when imaged with a NIR sensor.

Figure 1.10 shows an iris that is apparently devoid of textural morphology when imaged in the visible spectrum but that exhibits good textural patterns in the NIR spectrum. Since iris texture is believed to be unique, NIR cameras are typically used to acquire iris images for biometric purposes.



(a) Low melanin, Bluish (b) Moderate melanin, Yellowish (c) High melanin, dark brown

Figure 1.9 Example of blue, yellowish and dark brown iris images that contain low, moderate and high concentration of melanin, respectively.



(a) Dark iris (False color RGB)

(d)

(e)

Figure 1.10 Dark iris in (a) imaged at (b) 470nm, (c) 520nm, and (d) 700nm and (e) NIR wavelengths.

### 1.2.3 Pupil dynamics

Iris controls for the amount of *visible* spectrum light entering the pupil (lens). Although iris muscles are continuously adjusting for the light, they are usually maintained at a delicate balance with minimal movements. This state is known as the resting state of the eye. However external factors such as alcohol intake [24], change in brightness and administering eye drop drugs [25] and internal factors such as disease and stress forces either the sphincter or dilator muscles to activate, and to constrict or dilate the pupil accordingly.

Figure 1.11 shows examples of factors that influence pupil dilation/constriction.

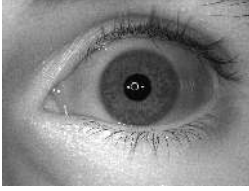
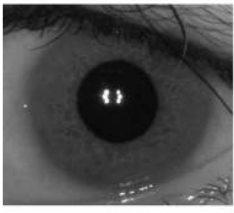
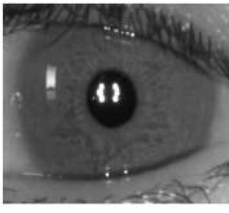
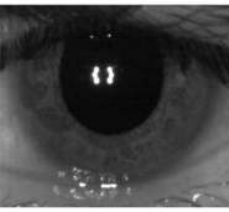
Before	Influence	After	Muscle
	Bright light on		Sphincter
	Visible light off		Dilator
	Drug (Eye drop) [25]		Dilator
	Alcohol Consumption [24]		Sphincter
	Alcohol Consumption [24]		Dilator

Figure 1.11 Examples of factors influencing the size of the pupil.

### 1.3 Iris biometric system

In reference to an iris biometric system, the biometric sensor is typically a NIR camera that acquires an image of an eye in the 750nm-850nm wavelength. It is then followed by a pre-processor module that consists of a segmentation process that identifies the iris region, and a normalization process that converts the annular region into a rectangular matrix. Feature extractor module encodes the iris texture and generates a template known as **IrisCode** that consists of binary values. These modules

are shown in Figure 1.12.

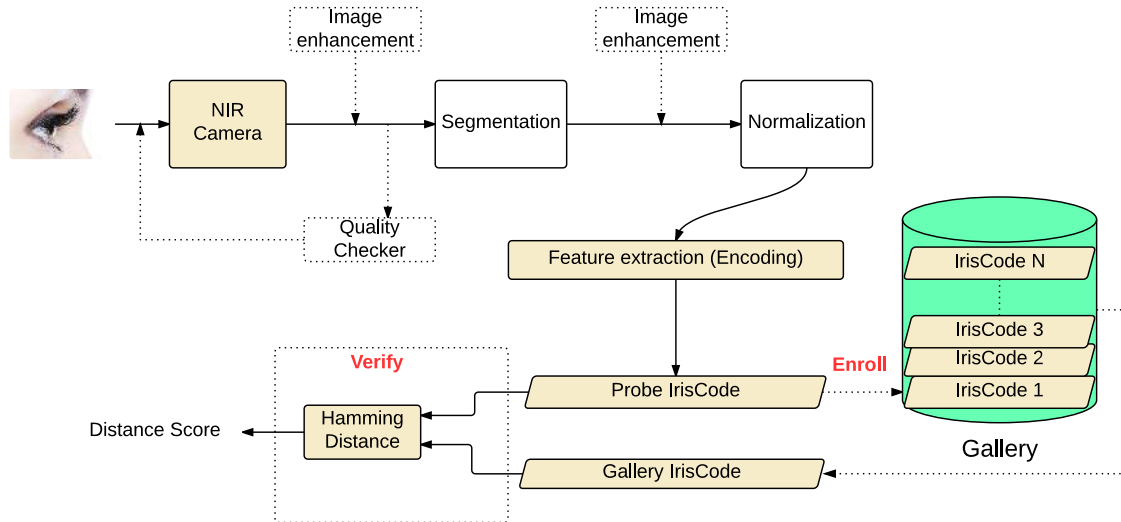


Figure 1.12 Components of a typical iris recognition system

Broadly, the components in Figure 1.12 may be categorized into the following tasks.

### 1. Image acquisition

Iris images are typically acquired in the NIR spectrum (750nm - 850nm). As described in the earlier section, the concentration of melanin pigmentation determines the perceived color of the iris in the visible spectrum. Higher concentrations of melanin results in darker colored irises while its absence results in lighter bluish iris colors. However, the effect of melanin decreases significantly in the NIR spectrum [17]. Hence, good textural patterns are observed, even for darker irises, in the NIR spectrum.

However, several works have argued for feasibility of iris image acquisition in the Visible spectrum [26][27] and Short Wave Infra-Red spectrum (900nm-1350nm) [28].

Traditionally, iris image acquisition required a subject to peer into the camera at close proximity. However, recently, there have been several systems that are able to acquire good

quality iris images “*at a distance*” [29][30] up to 3 meters or “*on the move*” [31]. There is also a system that is able to capture iris images as a person drives through a checkpoint [32]. There are other research efforts that aim to obtain consistently sharp images with good focus by extending the depth-of-field via wavefront coding [33] and hyper-focal imaging [34].

## 2. Segmentation

The acquired image consists of the ocular and periocular region. Segmentation is the process of automatically localizing the iris region in the given eye image. As part of this process, the inner pupillary boundary, the outer limbic boundary and the contours of upper and lower eyelids are detected. Occluding factors such as eye lashes and specular reflections are also detected.

There are various approaches to this segmentation task. Daugman, in [17], proposed an integro-differential operator that aims to find a boundary that has a maximum cumulative radial image gradient. The Integro-differential operator is given by

$$\max_{(r,x_0,y_0)} |G_{\sigma}(r) * \frac{\partial}{\partial r} \oint_{r,x_0,y_0} \frac{I(x,y)}{2\pi r} ds|.$$

The algorithm computes the cumulative radial image gradient at every pixel in the circumference of a circle with a fixed size radius. This process is repeated for multiple radius values,  $r$ . The circle that results in the maximum cumulative value is determined. This can correspond to the inner or outer boundary of the iris.

Wildes in [35] detects the edges in the images and converts the input image into a binary edge image. Then a circular Hough transform is used to identify circular boundaries. For a fixed acquisition distance, upper and lower limits can be set for the outer boundary radius. These limits are used to eliminate false positives and select the correct iris boundary. The region inside the outer boundary is then searched to find the inner pupillary boundary. Line Hough transform is used to detect upper and lower eyelids [36][4].

However, recent work in iris segmentation has focused on removing the assumption of circular boundaries, since the limbic and pupillary boundary are not typically circular under non-ideal conditions. Zuo and Schmid in [37] approximated the iris and pupil boundaries with more relaxed ellipses. Shah and Ross [38] further removed the constraints by first detecting the pupil by thresholding and then using a snake like geodesic active contour to find the limbic boundary. There are other similar work that rely on the principle of active contours [39][40], although the detection of pupil is still performed using basic thresholding followed by binary morphological operations, since its location is needed to initiate the active contour. Other methods involve classifying the pixels based on their textural content. Broussard et al [41] used a neural net to classify each pixel as iris or non-iris. These methods involve extensive training to build models that learn the difference between true iris pixels and non-iris pixels. He et al [42] used a trained AdaBoost detector to rapidly localize the iris region (rectangular bounding box).

### 3. Normalization

Normalization is the process of unwrapping the annular iris region into a fixed size rectangular grid. Normalization is expected to account for the iris texture deformation due to varying pupil size. Normalization is assumed to result in very similar rectangular images even if the images of the same eye are captured with different pupil sizes. However, recent works has shown the inadequacy of this assumption. Most methods are either based on or are variants of Daugman's rubber sheet model [17]. This step is *optional* since there are methods that perform image matching on the original images themselves such as [43], that used similarity of descriptors at local interest points, and [44], that used classic SIFT descriptor to match iris images.

The rubber sheet model maps each pixel  $(x,y)$  in the iris region to a point  $(r,\theta)$  in the

rectangular region using the following mapping function.

$$I(x(r, \theta), y(r, \theta)) \rightarrow I(r, \theta)$$

where,

$$x(r, \theta) = (1 - r)x_p(\theta) + rx_l(\theta)$$

$$y(r, \theta) = (1 - r)y_p(\theta) + ry_l(\theta).$$

Here,  $x_p(\theta), y_p(\theta)$  and  $x_l(\theta), y_l(\theta)$  are a set of pupillary and limbic boundary points. The formula can be interpreted as follows. The annular region is sampled at  $R$  regular intervals along the radial direction at a fixed angular value. The sampled points are assembled along a single column of the normalized image. This is repeated across multiple angular directions to populate other columns in the normalized image 1.14. Similarly, a normalized mask is also generated to denote the non-iris pixels that correspond to the eyelids, specular reflections, eye lids, etc.

#### 4. Pattern representation and matching

Since the iris texture is believed to be unique, there are several texture representation methods and corresponding distance measures to match two iris images. Classical method involves convolving the normalized image with a bank of complex Gabor filters of the form

$$G(r, \theta) = e^{-iw(\theta - \theta_o)} e^{-\frac{r(r-r_o)^2}{\alpha^2}} e^{-\frac{(\theta - \theta_o)^2}{\beta^2}},$$

where,  $r_o$  and  $\theta_o$  denote the radial and angular bandwidth of the 2-D Gabor filters. Figure 1.13 shows real and imaginary parts of a Gabor filter.

The real part of the resulting output is adjusted to have zero mean. Then the adjusted real part and the complex part are binarized depending on the sign of the response. Positive value is denoted as 1 and negative output is denoted as a zero. Hence, for each pixel in the normalized image, two bits are generated using one filter. The final binary representation of

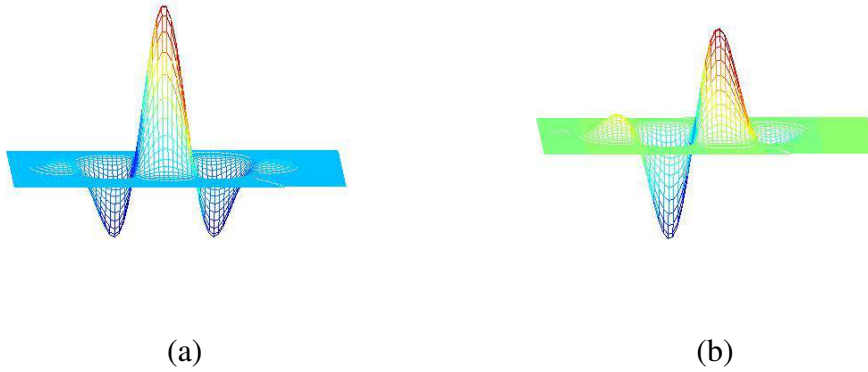


Figure 1.13 (a) Real part and (b) Imaginary part of a Gabor filter

the normalized iris image is referred to as *IrisCode*. IrisCodes  $C_A$  and  $C_B$  with corresponding masks  $M_A$  and  $M_B$  are compared using a fractional Hamming distance:

$$HD = \frac{(C_A \otimes C_B) \cap (M_A \cap M_B)}{\|M_A \cap M_B\|}.$$

In principle, this value may range from 0 (complete match) to 1 (complete mis-match). In practice, the impostor scores have a mean of 0.5 since the probability of two completely random bit-streams matching is around 0.5.

Other methods that use similar approaches include Boles and Boashash [45] that use zero crossing of 1D wavelet transform, Chou et al. [46] that uses Laplacian of Gaussian filters, Roche et al. [47] that use zero crossings of dyadic wavelet transform.

There are also methods that uses *eigen-iris* approach that attempt to extract basis functions and represent the input image as a combination of these basis functions. Examples include methods by Dorairaj et al. [48] who used PCA and ICA on the entire region, Huang et al. [49] who applied ICA on small windows, Ma et al. [50] who used Gabor filters in conjunction with Fisher's LDA to discriminate between iris images.

Other textural descriptors include GLCM (Gray Level co-occurrence Matrix) that was used by Chen et al. [51] in which they computed a 3-D co-occurrence matrix instead of the classic pairwise co-occurrence matrix. LBP (Local Binary Patterns) is also used to denote textural

patterns in non-overlapping blocks in the normalized image, and a block level similarity measure is used to compute distance measure.

Figure 1.14 shows the outputs of segmentation, normalization and encoding modules on a sample iris image.

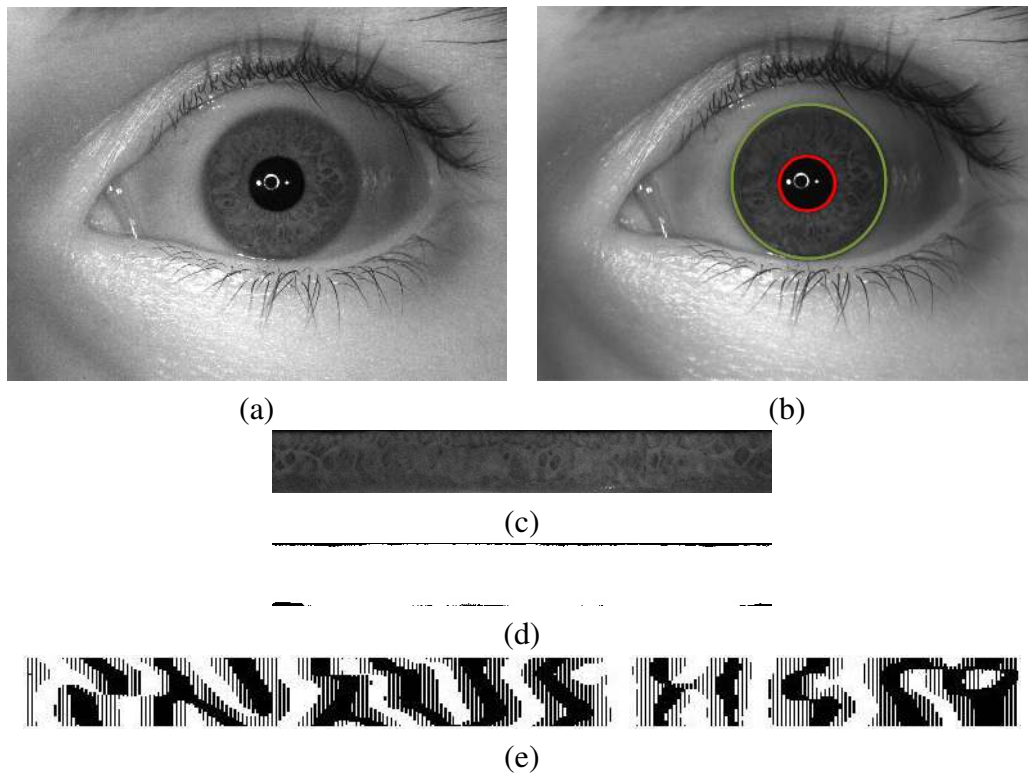


Figure 1.14 (a) Original acquired Image (b) Segmentation output (c) Normalized image (d) Corresponding mask image (e) IrisCode generated by encoding the normalized image using Masek's method. [4]

Other optional modules include quality checker to accept/reject the acquired images based on the quality of the acquired image, and a pre-processing module that enhances the quality of either the acquired images or the segmented iris texture.

## 1.4 Challenges in Iris recognition

There are multiple factors that influence the performance of an iris recognition system. Most of them are due to interaction between sensor and the user, while others are due to the characteristics of the eye and the choice of image processing methods. It may be noted that iris recognition systems have a very low False Match Rate (FMR) provided sufficient number of bits are matched (low occlusion). Hence, these challenging factors increase the False Non-Match Rate (FNMR) i.e, they result in failure of successfully matching images of the same eye acquired at different times. A list of such factors is presented below.

### 1. User Interaction and Ambient Factors

#### (a) Illumination

Poor illumination is not a major concern unless the illumination intensity is considerably low that results in the sensor registering dark noise instead of actual texture. However, non-uniform illumination is a very serious challenge. On the other end, strong illuminators can result in large specular reflections which might impact iris texture and, in some cases, affect segmentation accuracy. Figure 1.15 shows examples of poorly illuminated images.

#### (b) Occlusion

##### i Eyelids

Sometimes the users may not have their eyes completely open, see Figure 1.15, that would result in images where, iris is occluded by the eyelids. It reduces the number of iris pixels thereby reducing the discriminative power of the acquired image.

##### ii Eyelashes

Some individuals may prefer to have long and dark eyelashes [52]. Such eye lashes

can occlude a part of the iris. One of the major challenge here is to detect the eyelashes in order to exclude them during the matching stage.

iii Glasses

Although clear glasses are not believed to impact iris texture, it brings in additional challenges such as specular reflections and frame occlusions.

iv Contact lens

Certain types of contact lenses such as hard lenses, marked lenses and theatrical pattern contact lenses are shown to degrade iris performance by a considerable margin. However, it is possible to detect the presence of such contact lenses.

(c) Focus

Iris recognition systems expect a well focused image that has high frequency content in it. Strongly defocused images smooth out the texture and the resulting encoded information would correspond to the state of the sensor at the time of capture rather than the original texture [17]. However, it is easy to reject such kind of images by computing the focus measure rapidly in real time and retaining only in-focus images.

(d) Motion blur

Iris is located on a continuously moving organ known as the eye ball which is in turn placed in another moving object - the head. Hence, it is possible that the images procured by the camera exhibit a significant amount of motion blur.

(e) Image resolution

Typical iris image acquisition systems require the user to interact with the camera at close proximity. It ensures good image quality in terms of focus, blur and uniform illumination. But another major challenge associated with large standoff distance is poor image resolution. It is recommended to have at least 200 pixels across the iris diameter [53] to achieve good iris recognition performance.

(f) Off-axis iris image

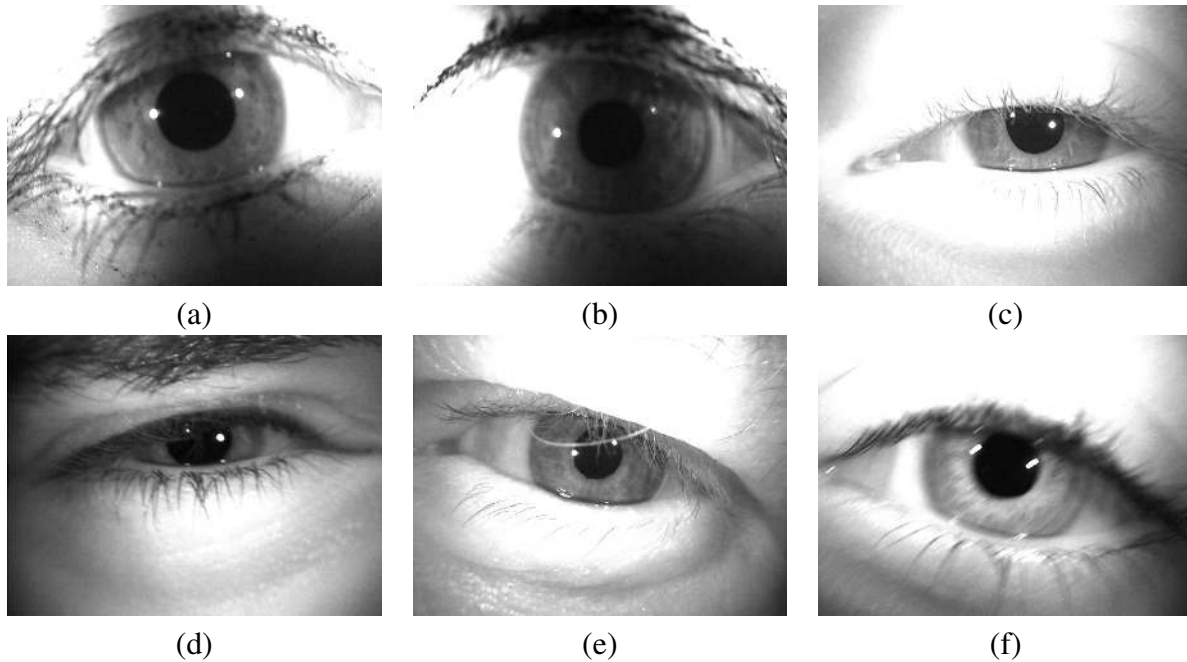


Figure 1.15 Examples of non ideal iris images. (a) and (b) Non-uniform illumination, (c) and (d) Eyelid occlusion, (e) Eyelash occlusion, (f) Motion blur.

Iris recognition systems require the captured iris image to be frontal, i.e, the eye has to be staring directly into the camera in line with its optical axis. Otherwise, the acquired image would be deviated from the optical axis in the roll, yaw and pitch directions. Figure 1.16 shows examples of few off-axis images. Off-axis images when compared

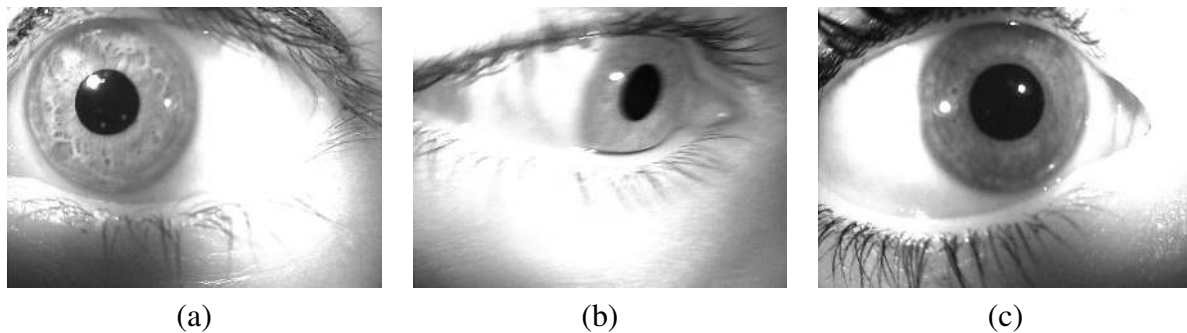


Figure 1.16 Examples of off-axis iris images.

against frontal enrolled images, would not yield the same normalized image nor can be compared directly since there is an affine transformation involved. Although such a transformation matrix may be estimated [16], it may not be complete and reconstruction

of one set of images from the other is not well-defined.

## 2. Sensor

It is possible for an iris to be enrolled using one camera sensor model but recognized using images acquired by a different camera sensor model. Bowyer et al. [54] observed that although the non-match distribution is stable, the match score distributions are adversely impacted.

## 3. Image compression

Biometric data may be stored digitally on passports. It is also sometimes necessary to store the original image rather than the IrisCode template. In some applications, this image has to be stored in limited space. For example, the Registered Traveller Inter-operability Consortium (RTIC) [55] allocates only 4000 bytes per eye. A typical gray scale iris image of size  $640 \times 480$  has 307,200 bytes of data that has to be compressed to 4000 bytes by a scale of 76.8. Rakshit and Monro [56] showed that the *normalized* or “unwrapped” iris image could be compressed to 2560 bytes and Daugman and Downing [57] showed that the original iris image (in native image domain) could be compressed to as low as 2000 bytes without substantially impacting the recognition performance.

## 4. Eye diseases

Eye diseases can adversely impact iris recognition [58][59][60] since they may deform the observed iris texture, distort pupil shape or impact eye color. Figure 1.17 shows examples of iris images exhibiting eye diseases. It can be observed that in some of the images, contours of the iris boundaries are drastically altered and textural abnormalities are induced.

## 5. Iris stability

Human iris starts forming from the third month of gestation. The constituent parts of the iris continue to grow and stabilize after 8 months of conception. However, the pigmentation continues to grow after birth until the second year. However, there are many theories for

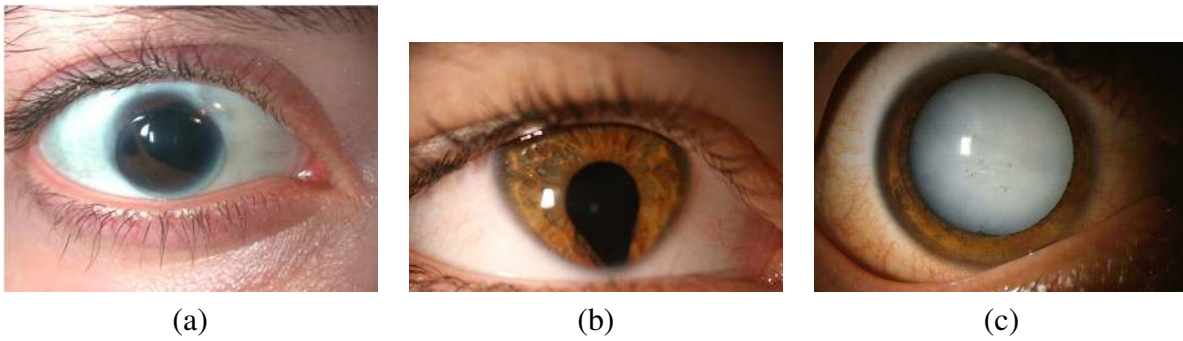


Figure 1.17 Few examples of eye diseases that impact iris recognition (a) Polycoria - Multiple pupil openings (b) Coloboma - Tear in iris (c) Severe cataract - Thickening of lens (looses transparency). Although the images are shown in RGB, some of these diseases can also impact the NIR images.

predicting the eye color given family history of eye colors [61]. It is commonly believed that the iris texture remains relatively stable (except in the case of the eye diseases) after two years since birth. However Fenker and Bowyer [62] have presented evidence of match score degradation when comparing images of the same eye taken two years apart using the same camera. This phenomenon is referred to as *iris aging*. It must be noted that iris aging may be, in part, due to the limitations of iris recognition algorithm and intra-class variation due to variations in pupil size and imaging conditions such as blur, focus and gaze directions across imaging sessions.

## 6. Pupil dilation

Pupil responds to the strength of light (in visible spectrum) entering the eye. It constricts in brighter light to protect the retina and dilates in darker environments to allow for more light to enter the eye. Daugman's rubber sheet model for normalizing the iris image [17] is believed to account for changes in pupil size across different lighting levels and image size. However recent research [6] has shown that extreme variation in pupil size would increase the Hamming distance between samples of the same eye resulting in false non-matches.

## 7. Multi-spectral matching

Although the iris is imaged in the NIR spectrum, there are practical benefits to be able to

perform iris recognition in visible spectrum especially due to the advent of smartphones that typically capture images in the visible spectrum. Also, Ross et al in [28] have shown the feasibility of performing iris recognition in wavelengths ranging from 900nm to 1350nm. These wavelengths are considered to be part of the Short Wave Infra Red (SWIR) spectrum. Human eye is not able to sense these wavelengths and a strong illuminator in SWIR band would be invisible to a human observer, making it viable for use in covert as well as nighttime environments. It is also sometimes required to match an iris image acquired in either visible or SWIR band against an NIR template stored in the database.

The major limiting factors to perform intra spectral or cross-spectral matching are

- Lack of textural content in darker iris when imaged in visible spectrum.
- Specular reflections in visible spectrum due to the tear film on the corneal layer.
- Differential response of iris constituents at different wavelengths.

## **1.5 Objectives of this work**

This work focuses on one of the major challenges facing iris recognition, namely *pupil dilation*. The adverse impact of pupil dilation is studied and a simple yet effective solution is proposed to improve the performance of iris recognition when the input images exhibit large difference in iris sizes.

## CHAPTER 2

### MOTIVATION AND PREVIOUS WORK

Iris is a complex structure in the human eye that has very interesting elastic properties. When the light incident on the eye is varied, muscles in the iris contract or expand to allow for less or more light into the eye to better perceive the scene whilst protecting the retina at the same time. Interestingly, the iris muscles revert exactly to their old position after a perturbation [63].

#### 2.1 Motivation

During the normalization stage, most iris recognition algorithms unwrap the iris into a pseudo-polar coordinate rectangle using Daugman's rubber sheet model [17] by sampling the iris region uniformly along the radial and angular directions. This transformation is believed to account for changes in iris size due to its compression or dilation. However, upon simple visual observation, it is evident that iris undergoes a complex non-linear deformation during pupil constriction or dilation. It is well documented that extreme pupil dilation affects the match score between two iris images [6]. Larger the pupil size difference between two images of the same iris, larger is the Hamming distance. Figure 2.1 shows (a) an eye image and (b) its corresponding normalized iris image [5]. When the pupil dilates from (a) to (c), the iris region is compressed in a non-linear fashion as shown in (d). Close-up of regions in Figure 2.1 (b) and (d) shows that these highlighted regions do not align well with each other.

Hollingsworth et al. [6] showed that a large difference in pupil size between two images results in a large genuine dissimilarity score. Figure 2.2 shows two iris images with different pupil-to-iris radius ratio values. If the dilation ratio is defined as the ratio of pupil radius to iris radius, then a smaller value of pupil dilation ratio indicates a larger iris region with a smaller pupil size relative to the iris radius and a larger dilation ratio indicates a larger pupil size with relatively less iris region. It is not uncommon to find iris images that have dilation ratios as low as 0.2 and as high as 0.8 [6].

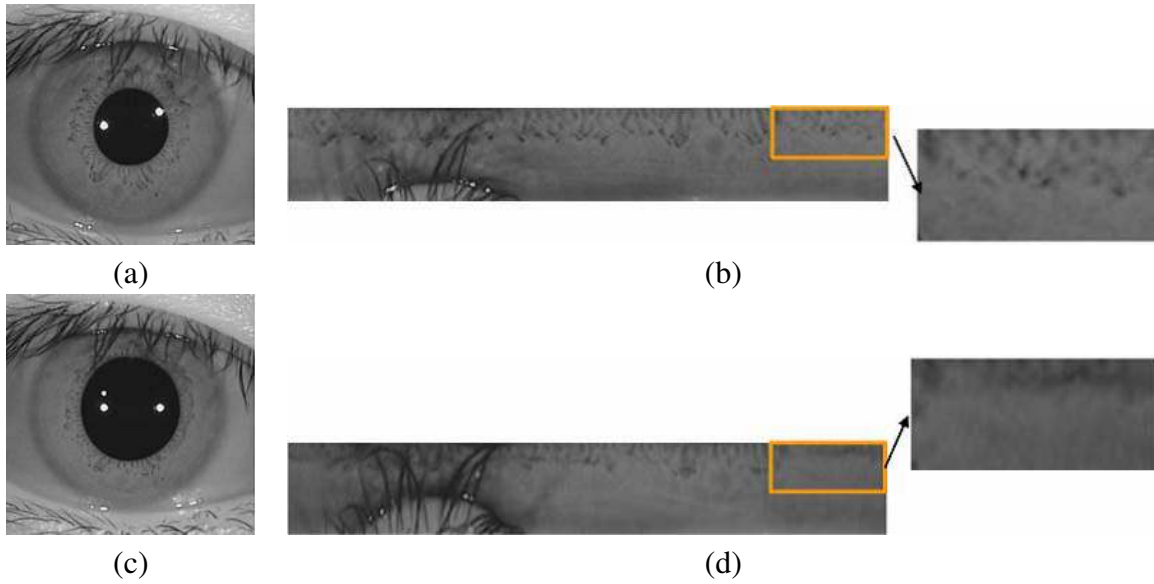


Figure 2.1 (a) and (b) Iris image with moderate pupil size and the corresponding normalized iris image. (c) and (d) Iris image with large pupil size and the corresponding normalized iris image. Highlighted regions in (c) and (d) do not align correctly. Images from [5].

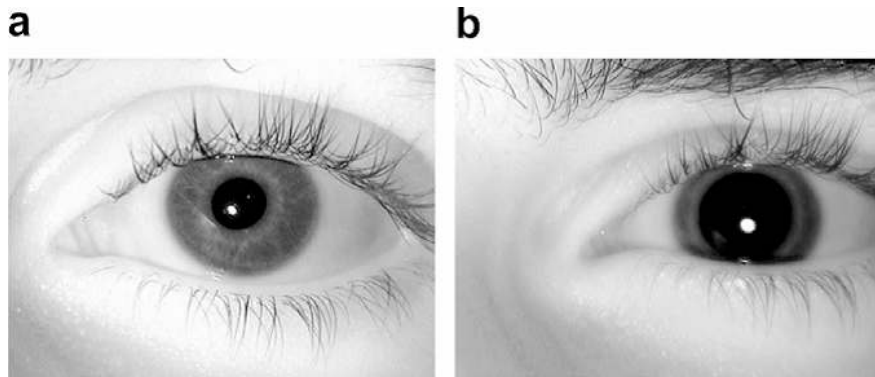


Figure 2.2 Iris images with dilation ratios of (a) 0.3478 and (b) 0.6545. Images from [6].

In effect, the eye image acquired at different times can exhibit a large variation in dilation ratio, thereby increasing the possibility of false non-matches, where the user is failed to be identified.

Hence, there is a need to account for the variations in iris texture to better match two iris images with large pupil size variation.

## 2.2 Previous work

The previous work on this topic may be broadly divided into three categories based on their end goals. The first line of work tried to model the dynamics of iris deformation by deriving a theoretical model to understand the deformation process. The second line of work only emphasized on improving the iris matching performance in presence of pupil dilation without necessarily modeling the biological basis. The third category of work only focused on documenting the effects of pupil dilation.

The following are three deformation models proposed in the literature in chronological order.

1. Minimum wear and tear model;
2. Empirical model;
3. Mechanical strain model.

### 2.2.1 Minimum wear and tear model

Rohen [7] was the first to propose a structure for collagenous fibers in iris. Figure 2.3 shows the structure proposed by [7] that consists of orthogonal set of fibers (clockwise and anti-clockwise) that connect the pupil boundary to the outer iris boundary. Rohen also observed that these fibers are interwoven with blood vessels and other components of the iris.

#### 2.2.1.1 Wyatt 2000

Wyatt [8] provided a mathematical framework for this meshwork that minimizes *wear and tear* of iris muscles due to constriction or dilation. There are additional constraints that have to be satisfied for better application of this model for iris deformation. For example, points on the iris should not rotate too much around the center of pupil as the pupil diameter increases. Secondly, the fiber arcs in the meshwork must not have relative slip at any given location. The conditions laid by the

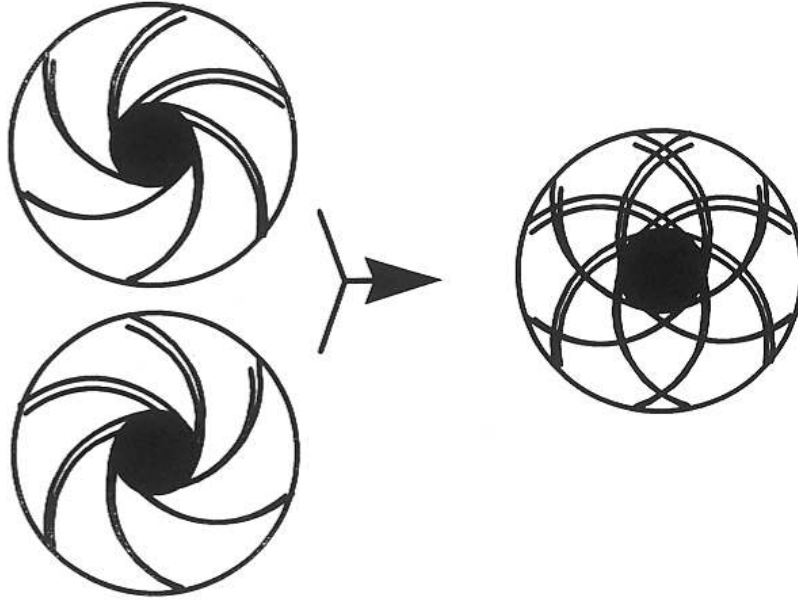


Figure 2.3 Iris mesh work proposed by Rohen [7]. Image from [7].

constraints are met when points in the iris region are assumed to move only in radial direction as pupil diameter varies.

Wyatt modeled linear deformation of iris according to the following formula

$$R(\theta, \theta_o, p) = R(\theta, \theta_o, p_{ref}) \left( \frac{r_o - p}{r_o - p_{ref}} \right) + r_o \left( \frac{p - p_{ref}}{r_o - p_{ref}} \right).$$

$R$  is the radius as a function of polar coordinate  $\theta$ , the polar angle traversed by a single fiber from pupillary margin to the iris root  $\theta_o$ , and pupil diameter  $p$ ; the meshwork is initialized with the pupil diameter equal to  $p_{ref}$ . Figure 2.4 shows a pictorial representation for  $\theta_o$ .

The meshwork was represented using a simple logarithmic spiral of the form

$$R = p \left( \frac{R_o}{p} \right)^{\left( \frac{\theta}{\theta_o} \right)}.$$

After solving for logarithmic spirals, additional deviation was allowed in the form of a 20-term polynomial in  $\theta$  to account for nonlinear deformation. An optimum curve was found for  $\theta = 100^\circ$  as shown in Figure 2.5. The nonlinear stretch of iris is modeled as the sum of a linear stretch and

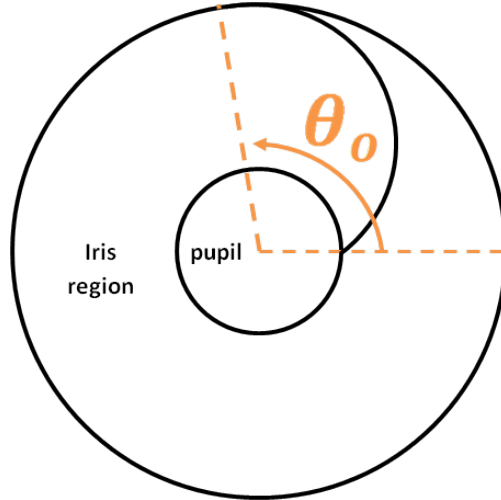


Figure 2.4  $\theta_0$  is the angle between starting point of the fiber arc on pupillary boundary and ending point on limbic boundary.

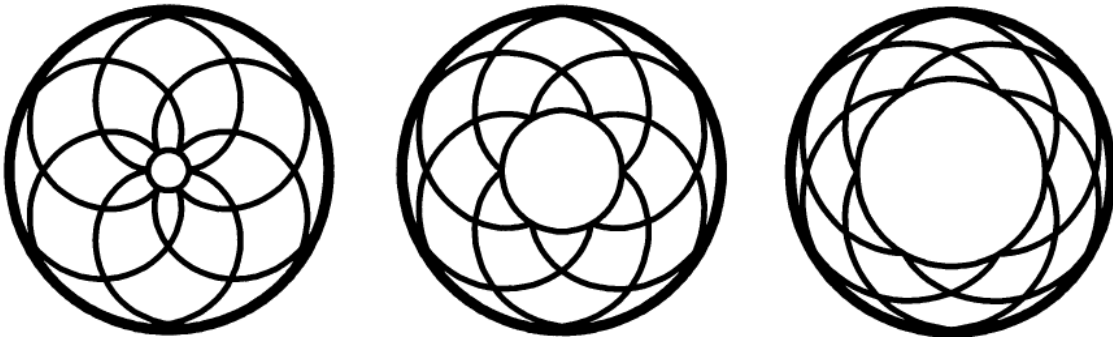


Figure 2.5 Optimum arcs derived by Wyatt [8] for  $\theta = 100^\circ$ , and pupil diameter 1.5, 4.0 and 7.0 mm

a nonlinear deviation.

$$R = R_{linear} + \Delta R(p, r).$$

where,  $R_{linear}$  is the solution of the linear deformation model and  $\Delta R$  is the additional displacement of a point on the iris region after the linear stretch.  $\Delta R$  is approximated using a 6<sup>th</sup> order polynomial.

### 2.2.1.2 Yuan and Shi 2005

Yuan and Shi [9] leveraged the idea of meshwork as fibers, and described a model for estimating the location of a point in the iris region after deformation. Semi-circular arcs are constructed as shown in Figure 2.6. From the figure,  $P'$  is the reference pupil boundary which is deformed to the

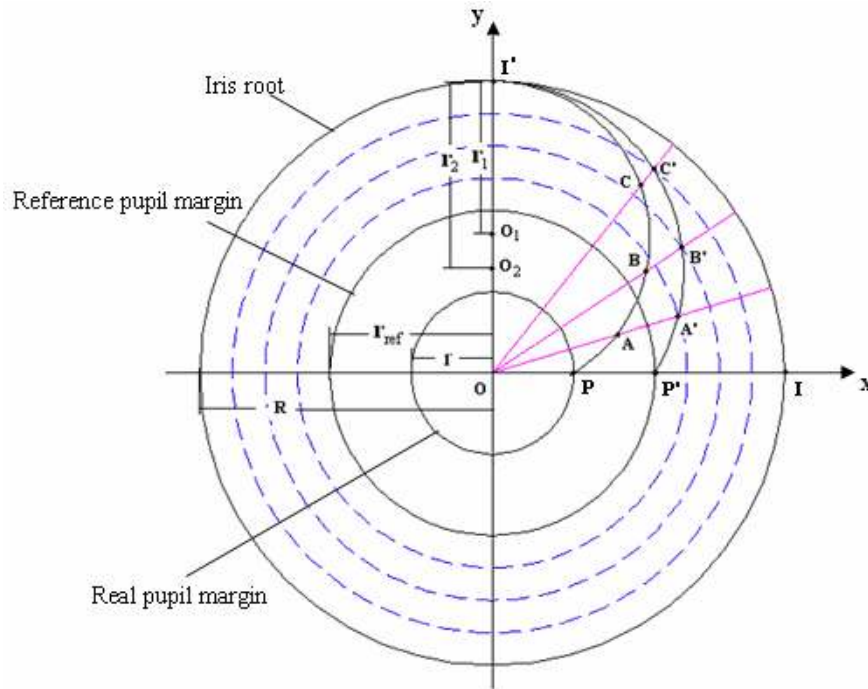


Figure 2.6 Normalization model proposed by Yuan and Shi. Image from [9].

current boundary marked as  $P$ .  $I'$  is the iris root boundary which is assumed to remain fixed. In this implementation, the angle between any  $P$  and it's corresponding  $I'$  is  $\pi/2$ . The arcs before and after deformation are modeled as sectors of circles. Given a location  $A'$  in the iris region of the reference image, it's corresponding location  $A$  after deformation can be easily derived as a function of the point's location with respect to the pupil center. The assumptions made in this model are:

- the pupillary and limbic boundaries are approximated as concentric circles;
- margin of the pupil (boundary) does not rotate significantly; and
- shape of pupil remains roughly circular during dilation or constriction.

From the model, it is evident that points closer to the pupil boundary are displaced by a large distance, while points closer to the iris root (limbic boundary) are not displaced as much. This introduces a nonlinearity in displacement magnitudes for points in the iris region as a function of their distance from the pupillary boundary. A parameter  $\lambda$  is defined as

$$\lambda = \frac{r}{R},$$

where,  $r$  is the radius of pupil and  $R$  is the radius of the outer iris boundary. As in the previous model, a fixed pupil radius is chosen as the reference using the formula  $r_{ref} = \lambda_{ref} * R$ . The deformation model is used to deform the given iris as its pupil radius changes from  $r$  to  $r_{ref}$ . Once the given iris image is deformed to match pupil radius equal to  $r_{ref}$ , then it is linearly mapped to a pseudo-polar rectangular grid using Daugman's method [17] for further encoding and matching.

### 2.2.1.3 Wei et al. 2007

The model proposed by Wei et al. [5] follows along the same lines as Waytt [8] by modeling the nonlinear stretch of points in iris regions as sum of a linear stretch and a deviation. This deviation is modeled as a function of the current pupil radius,  $p$  and position,  $r$ :

$$R_{nonlinear} = R_{linear} + \Delta R(p, r).$$

While Waytt [8] approximated the deviation value as a 6<sup>th</sup> order polynomial in  $\theta$ , Wei et al. computed the deviation values using statistical measures of a training set.

As the iris radius may differ slightly depending on the relative position of the eye to the camera during image acquisition, a consistent parameter called iris deformation factor  $T$  is defined as

$$T = \frac{R_p}{R_i},$$

where,  $R_p$  and  $R_i$  are radius of the pupil boundary and the iris root boundary, respectively.

$\Delta R$  is then modeled as a function of  $R_{linear}$  and  $T$ ,

$$R_{nonlinear} = R_{linear} + \Delta R(R_{linear}, T).$$

This iris deformation factor,  $T$ , is same as the dilation ratio in [6].

A reference band for  $T$ , namely  $[T_s, T_l]$ , is chosen and the deformation model is applied when the value of  $T$  is outside this band. The pupil is dilated for  $T > T_l$ , and the pupil is constricted for  $T < T_s$ . The deviation from the linear stretch is a factor of how far  $T$  is from the reference band. The deviation from linear stretch is formulated as

$$\Delta R = C \times F(R_{linear}),$$

where,  $C = (\frac{T_s+T_l}{2} - T)$  and  $F(R_{linear})$  is a function of the linear stretch,  $R_{linear}$ . Here,  $C$  determines the strength of nonlinear deformation.

$F(R_{linear})$  is learnt using a training set of 600 iris images from 60 subjects with 10 samples each, that were obtained at gradually varying illumination. A set of points in the iris region are manually marked and tracked across the 10 images. The set of points are divided into three regions,  $\{P_{in}\}, \{P_{mid}\}$  and  $\{P_{out}\}$ , based on their proximity to the pupil boundary using nearest neighbor clustering. Nonlinear stretch is computed for these three regions and deviation  $\Delta R$  is derived for all the three regions. The plotted deviations for these regions are approximated using Gaussian distributions.

$$\begin{aligned} \Delta R &= C \times F(R_{linear}) = C \times N(\mu, \sigma^2) \\ &= C \times \frac{1}{\sqrt{2\pi}\sigma} \exp \left\{ -\frac{(R_{linear} - \mu)^2}{2\sigma^2} \right\}. \end{aligned}$$

Parameter  $C$  is the iris deformation factor that can be estimated from the iris image.  $(\mu, \sigma)$  can be estimated from plots of deviations.

## 2.2.2 3-D anatomical model

### 2.2.2.1 Francois et al. 2007

This is not an iris deformation model but an anatomical representation of the iris structure that could potentially be used to model iris deformation. Iris is a 3-D entity consisting of structures

at different depths from the corneal plane. The incident light is refracted onto these structures and a 2-D projection on the recording camera is visualized as an image. Francois et al. [64] proposed a method to recover structure of iris from a single photograph. A representation known as Subsurface Texture Mapping [65] is used to describe the morphological relief of the human iris. Then a refractive function is also presented to account for refraction at corneal surface.

### 2.2.2.2 Clark et al. 2012

The mechanical model proposed by Clark et al. [66] considers iris as a material that is acted upon by internal mechanical forces, and subsequent deformation is modeled in terms of mechanical strain, stress and material properties of iris. A mathematical model is derived using biomechanics of iris to characterize the nonlinear deformation.

The iris is approximated as a thin cylindrical shell with negligible thickness in the  $z$  direction and the structure reduces to a thin plate and can be modeled in terms of polar coordinates  $r$  and  $\theta$ . The displacement of a point in the iris region, when the pupil radius changes from some initial value to some final value, is represented as  $u(r, \theta)$ .

$$\vec{u}(r, \theta) = u_r * \vec{r} + u_\theta * \vec{\theta}.$$

Cauchy-Euler equations [67] for thin plates are used for strain equilibrium conditions while a separate set of stress equilibrium conditions are also derived.

Additional assumption of negligible angular displacement,  $u_\theta$  and  $\frac{\partial}{\partial \theta}$ , is made based on the observation that pupillary response causes axisymmetric load on the iris muscles and that iris muscles are equally distributed across the iris region. These assumptions also lead to the nullification of shear stress [68]. Now, the displacement vector becomes  $u = u_r * \vec{r}$ . The reduced equilibrium conditions based on additional assumptions are as follows:

- For strain:

$$\varepsilon_r = \frac{du}{dr} - \frac{1}{2} \left( \frac{du}{dr} \right)^2. \quad (2.1)$$

$$\varepsilon_\theta = \frac{u}{r} - \frac{1}{2} \left( \frac{u}{r} \right)^2. \quad (2.2)$$

- For stress:

$$\frac{d\sigma_r}{dr} + \frac{\sigma_r - \sigma_\theta}{r} = 0, \quad (2.3)$$

where,  $\varepsilon_r$  and  $\varepsilon_\theta$  are normal strains;  $\sigma_r$  and  $\sigma_\theta$  are normal stresses, respectively.

Relation between the strain vector and the stress vector is computed assuming the iris material to be orthotropic that can be deformed only in two orthogonal directions ( $r$  and  $\theta$  in this case).

$$\varepsilon_r = \frac{\sigma_r}{E_r} - \frac{\nu_{r\theta}}{E_\theta} \sigma_\theta, \quad (2.4)$$

$$\varepsilon_\theta = -\frac{\nu_{\theta r}}{E_r} \sigma_r + \frac{\sigma_\theta}{E_\theta}, \quad (2.5)$$

where,  $E_r$  and  $E_\theta$  are Young's moduli of elasticity for iris;  $\nu_{r\theta}$  and  $\nu_{\theta r}$  are Poisson's ratio of the iris material in the azimuthal and radial directions, respectively. The symmetry property for orthotropic material states that

$$\frac{\nu_{\theta r}}{E_r} = \frac{\nu_{r\theta}}{E_\theta}. \quad (2.6)$$

Substituting equations 2.4 and 2.6 in equations 2.1 and 2.3 gives rise to a master differential equation of the form,

$$u'' + \frac{u'}{r} - \frac{\zeta u}{r^2} - \frac{(1 - \nu\zeta)}{2r} (u')^2 - \frac{(\nu - 1)\zeta}{2r} \left( \frac{u}{r} \right)^2 - \frac{1}{2} \frac{d}{dr} (u')^2 - \frac{\nu\zeta}{2} \frac{d}{dr} \left( \frac{u}{r} \right)^2 = 0, \quad (2.7)$$

where,  $()'$  is regular differentiation w.r.t  $r$ ;  $\zeta = \frac{E_\theta}{E_r}$  and  $\nu = \nu_{\theta r}$ .

Equation 2.7 is solved as boundary value problem with conditions

$$u(\text{pupil\_boundary}) = c$$

and

$$u(\text{limbic\_boundary}) = 0.$$

Here,  $c$  is the difference in pupil radius between the initial and final configuration. Another key assumption in boundary values is that iris remains fixed at the limbic boundary. That is, displacement of points on the limbic boundary is zero. The master differential equation is solved using the finite element method and numerical results show a nonlinear deformation of the iris region with variation in pupil size. They also show the solution for the master equation along with numerical results and simulation whilst assuming that the iris region is isotropic. Isotropic deformation is considered to be a special case of orthotropic deformation when  $E_r = E_\theta$ . In their work it is observed that linear deformation is a good approximation for nonlinear deformation in case of smaller changes in pupil size, but a strong nonlinear deformation is clearly evident when the pupil size changes by a large magnitude.

### **2.2.3 Gejji et al. 2015**

Gejji et.al in [69] and Clark et.al in [70] studied the response of pupil to light, also known as pupil light reflex (PLR), in the near infra-red (NIR) spectrum using a biological model.

### **2.2.4 Other Deformation models**

All the aforementioned models assume that the iris is a 2-D structure and that angular displacement is negligible. However, iris is in fact a 3-D structure and the image acquired is only a 2-D projection of the texture. Therefore, there is a need to model the iris deformation as a 3-dimensional object. Additional structures such as contraction furrows become evident when the iris is compressed. It is still very complex to model the iris as a 3-D deformable object since no information is available in the 3<sup>rd</sup> dimension. There are several deformation models in the literature that can potentially be used to model the iris deformation such as (a) dynamic modeling of local and global deformation [71], (b) utilizing principles of deformations of elastic material from continuum mechanics [72], (c) modeling using splines and their variants [73], and (d) developing models using fixed anchor points around which deformation occurs.

Several papers have been published that describe the improvement of performance of iris matching between eye images of varying pupil sizes. For example, Yuan and Shi [9] used the minimum wear and tear model to derive an equation that predicts the exact location of a point in the iris region after dilation. In another work, Wei et al. [5] approximated the non-linear term in Wyatt's model  $\Delta R(p, r)$  using a Gaussian distribution that is in turn learned from a training set. Thornton et al. [74] divided the normalized iris into a set of non-overlapping blocks, and computed transformation parameters between corresponding blocks in the target image. Then the posterior probability of these parameters is maximized iteratively resulting in the optimal deformation parameter set. This information is used to compute block-wise similarity metrics that are averaged to produce a final score. Tomeo-Reyes et.al [75] used the bio-mechanical iris tissue model used in [66] to predict the displacement of a point in the iris at a given dilation level and used this in the normalization process. They tested their technique on the WVU-PLR dataset to show a significant improvement in matching performance especially when comparing iris images with large variation in pupil sizes.

Pamplona [25] collected extremely dilated images of a few eyes by administering mydriatic drugs that dilated the pupil. Specific points in the iris region were then manually annotated and tracked across the images. It was observed that points are displaced predominantly in the radial direction and structures such as crypts deform in the angular direction. There are several papers [6][76][77] that demonstrate the adverse impact of pupil dilation on iris matching performance.

### **2.3 Bit matching**

There have been other methods developed that exploit the characteristics of the IrisCode to improve the performance of an iris recognition matcher. Hollingsworth et al. [78] used a matching scheme where only best bits in an IrisCode are used. Best bits are chosen based on their consistency across different samples of the same eye. Rathgeb et al. [79] employed a selective bit matching scheme by comparing only the most consistent bits in an IrisCode. These consistent bits are obtained by using

different feature extractors. In other works, Rathgeb et al. [80] proposed a new distance measure based on Hamming distance values that are generated by shifting one IrisCode with respect to the other at multiple offsets. In SLIC [81], IrisCodes are matched one row at a time, thereby decreasing the discriminatory potential of IrisCodes that are typically matched in their entirety but resulting in better match speeds.

## CHAPTER 3

### COLLECTION OF DATABASE

#### 3.1 Motivation

Major drawbacks of the previous work in the literature to address the problem of pupil dilation are as follows. 1) Theoretical models are not empirically validated; 2) Software solutions require significant alterations to existing systems; and 3) Datasets used in previous research do not systematically measure the impact of pupil dilation on iris matching. Previously demonstrated effects of pupil dynamics were tested on generic datasets that were not specifically acquired for studying the effect of pupil dilation. As noted earlier, there are several other contributing factors such as focus, illumination changes and blur that can impact recognition accuracy. In our work, these factors are overcome by acquiring a dataset in highly *controlled* illumination conditions and distances as described in the following section.

#### 3.2 Data acquisition protocol

Videos are captured with a Redlake (DuncanTech) MS3100 multispectral camera at roughly 8 frames/s and saved as a sequence of still images. The camera is attached to the mobile arm of an ophthalmologist's slit lamp and connected to an Epix frame grabber. An annular ring light flanked by 2 NIR LEDs (810 nm) is placed in front of the camera and is connected via an optic fiber guide to a StellarNet light source (a voltage regulator and a tungsten-krypton bulb with a broad spectrum of 300 nm to 1700 nm). The two LEDs are used for an even illumination of the eye while camera is focused prior to data collection. With the chin on the chin rest and gazing into the camera, the participant is given time to adjust to the darkness. With camera in focus, the recording is started. After 10 seconds, the on/off button on the light source panel is turned on, the light is directed to the eye through the annular ring for an additional 10 seconds interval of time, after which the light

is turned off. The video recording is stopped following 10 seconds of darkness. The NIR LEDs are on for the duration of the recording. The video captures the pupil dynamics: the constriction of the pupil when the eye is exposed to the flash of light and the dilation of the pupil when the eye adapts to the darkness. Figure 3.1 depicts the variation of the voltage on the tungsten-krypton bulb. The camera acquires color infrared images (CIR) with a resolution of 1040x1392x3 pixels that includes NIR spectrum as well as visible light spectrum.

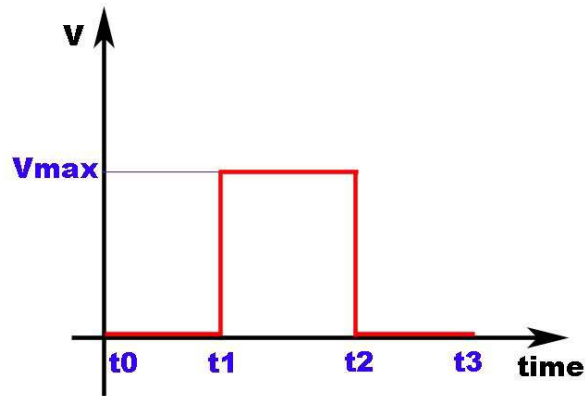


Figure 3.1 Image sequence capture starts at  $t_0 = 0$ . After approximately 10 seconds, at  $t_1$ , the light source is turned on illuminating the eye for 10 more seconds  $[t_1, t_2]$ . At  $t_2$  the light source is turned off and remains off for 10 more seconds  $[t_2, t_3]$ . The video capture is stopped at  $t_3$ .

### 3.3 Description

The data is collected from 54 subjects, one video/eye with an average of 130 frames / video. The total number of images is 7115 for the left eye and 6985 for the right eye with an average of 440 pixels across the iris diameter.

Example of NIR images are shown in Figure 3.2. Distribution of demographics and eye color information is presented in Tables 3.1 and 3.2.

Relation between pupil radius ( $R_P$ ) and iris radius ( $R_I$ ) may be represented as a difference,  $D$ , or a ratio,  $R$ ; where

$$D = R_I - R_P,$$

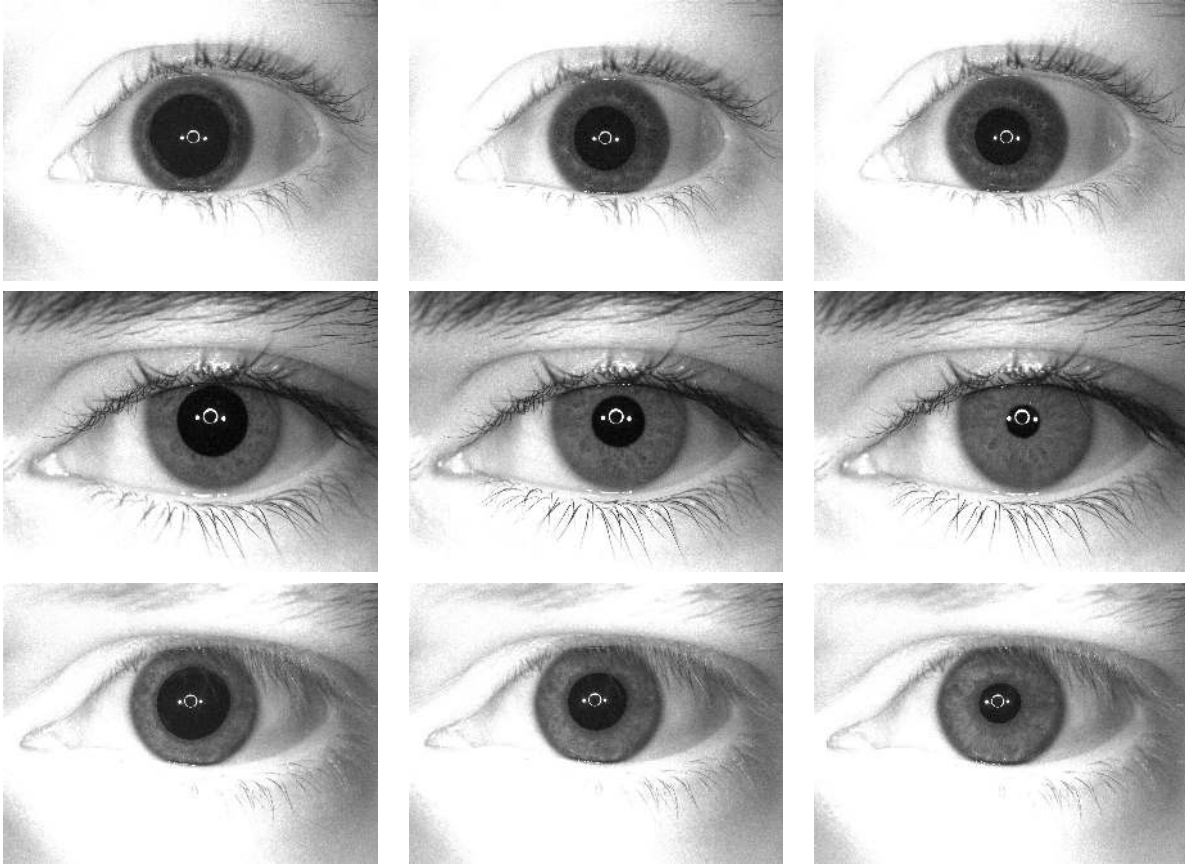


Figure 3.2 Sample images from the dataset

Table 3.1 Demographics distribution

Demographics	
Caucasian	32
Asian	20
African	1
African American	1

Table 3.2 Eye color information

Eye Color	
Blue	7
Green/Hazel	6
Light Brown/Mixed	4
Brown	10
Dark Brown	27

$$R = \frac{R_P}{R_I}$$

$R$ , is usually known in the literature as *pupil dilation ratio*. The iris radius does not change for all the eyes even when the pupil is undergoing dilation and constriction. Hence, only the pupil size is found to vary when the light source is turned on or off. Figure 3.3 shows the histogram of pupil dilation ratio of a subset on 2218 images corresponding to the left eye in the dataset.

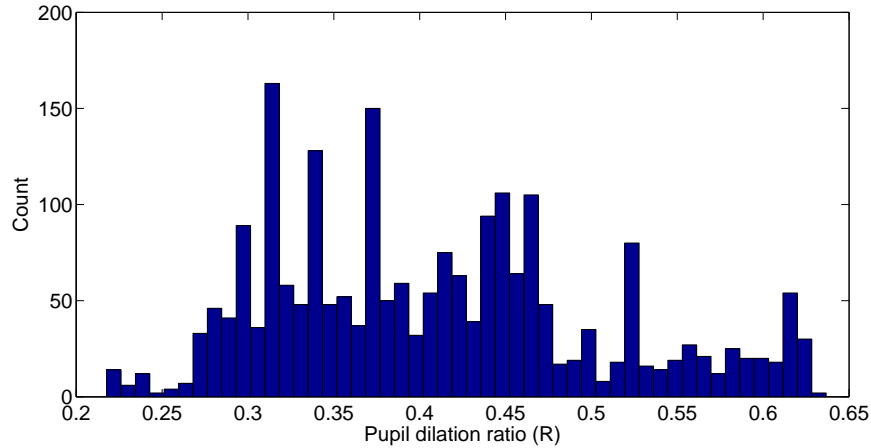


Figure 3.3 Distribution of pupil dilation ratios in the dataset. They range from 0.2177 to 0.6367.

### 3.4 Impact of pupil dilation

Pupil dilation is known to impact iris matching systems by increasing the Hamming distance between images of the same eye having different pupil sizes. Genuine scores are computed for images of the same eye at different pupil sizes in order to study the impact of pupil dilation. Relation between the pupil and iris radius for images  $I_1$  and  $I_2$ , denoted as  $(D1, R1)$  and  $(D2, R2)$ , respectively, can be computed as follows:

$$D1 = R_{I_1} - R_{P_1},$$

$$D2 = R_{I_2} - R_{P_2},$$

$$R1 = \frac{R_{P_1}}{R_{I_1}},$$

$$R2 = \frac{R_{P_2}}{R_{I_2}}.$$

Figure 3.4 shows the distribution of *genuine* Hamming distance scores as a function of (a)  $|D1 - D2|$  and (b)  $|R1 - R2|$ . Typical iris radius is around  $6mm$ . The difference in iris widths and dilation ratios are scaled with respect to  $6mm$  iris radius and three different categories of

dilation differences/ratios are considered. The boundaries between these categories correspond to approximately  $0.5\text{mm}$ ,  $1\text{mm}$  and  $> 1\text{mm}$  deformation in pupil radius.

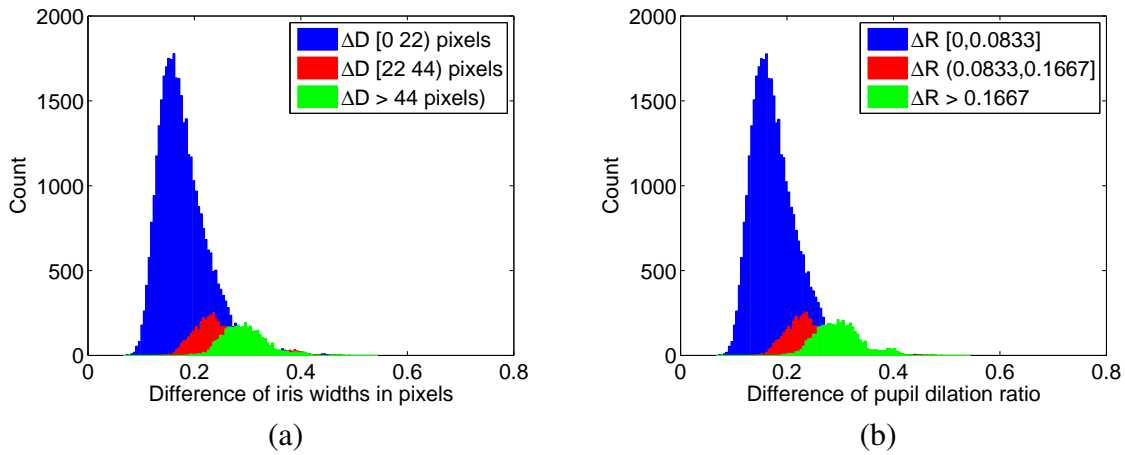


Figure 3.4 Distribution of genuine Hamming distance scores as a function of dilation differences. (a)  $|D1 - D2|$  and (b)  $|R1 - R2|$

It can be observed from all the plots in Figure 3.4 that, in general, larger differences in iris widths or pupil dilation ratios result in a larger Hamming distance when matching iris images of the same eye. This substantiates the previous findings of pupil dilation's adverse impact on iris matching systems.

## CHAPTER 4

### PROPOSED METHODS

The proposed methods require iris to be encoded using different filters of varying bandwidths. In this work, unwrapped iris regions are encoded using multi resolution Gabor filters. This section describes the encoding process to generate IrisCode; the methodology used by typical iris matchers to generate match scores; followed by the proposed novel matching method and how it is different from the typical matcher.

#### 4.1 Multi-resolution Gabor filter encoding

IrisCodes can be generated by applying multi-scale filters on a normalized iris image and quantizing their complex output. One such implementation by OSIRIS applies filters of three different sizes. Each filter produces two bits of IrisCode per pixel.

Let the  $i^{th}$  image be denoted by  $I_i$ . Its normalized image is denoted as  $N_i$ . The size of the normalized image is  $r \times t$  where  $r$  is the radial resolution and  $t$  is the angular resolution. Three rectangular complex filters  $F_{m_1 \times n_1}^1$ ,  $F_{m_2 \times n_2}^2$  and  $F_{m_3 \times n_3}^3$  are applied on the normalized image. The resulting complex output is then converted to a binary IrisCode set  $(C_i^1, C_i^2, C_i^3)_{r \times 2t}$  along with a mask  $M_{i_{r \times 2t}}$ . Figure 4.1 pictorially shows an IrisCode set.

Normalized image with size  $r = 64$  and  $t = 512$  for filter sizes  $9 \times 15$ ,  $9 \times 27$  and  $9 \times 51$  are used in this work. Figure 4.2 shows a normalized iris image and its corresponding IrisCode generated using the 3 complex filters. The smallest filter encodes smaller regions in the image and the largest filter encodes larger regions in the image. This is reflected in the smoothness of IrisCodes at different filter sizes. The larger filter results in a smoother IrisCode compared to the smaller filter.

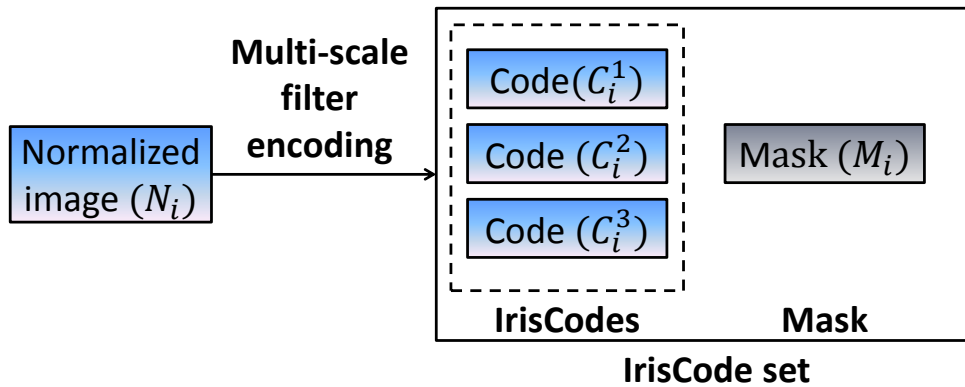


Figure 4.1 A normalized image is encoded using multi-scale filters to result in an IrisCode set along with a mask showing valid bits in each IrisCode. This mask is same for all the codes in the IrisCode set

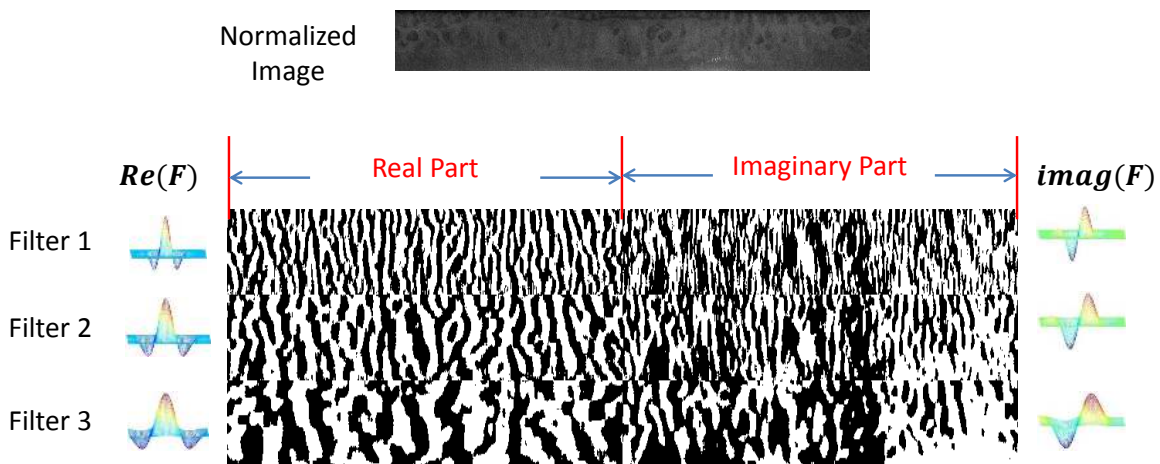


Figure 4.2 A normalized image and its corresponding IrisCode generated using 3 filters. These filters encode the image at multiple scales.

## 4.2 Typical IrisCode matcher

Let us suppose that IrisCode sets generated from two normalized images  $N_i$  and  $N_j$  are being matched. The corresponding IrisCode sets are represented by  $(C_i^1, C_i^2, C_i^3, M_i)$  and  $(C_j^1, C_j^2, C_j^3, M_j)$  respectively. A common mask,  $M_{ij}$  is computed to denote the location of common valid bits corresponding to the iris in both the IrisCodes.

$$M_{ij} = M_i \cap M_j.$$

Let the result of XOR operator,  $\otimes$ , for matching individual IrisCodes generated by filter  $F$  be  $R^f$ :

$$R_{ij}^f = C_i^f \otimes C_j^f, f = 1, 2, 3.$$

$\otimes$  results in 0 if the corresponding bits are the same and 1 if they are not. Hamming distance between two IrisCodes at the  $f^{th}$  filter scale is then given by

$$HD_{ij}^f = \frac{\|R_{ij}^f \cap M_{ij}\|}{\|M_{ij}\|}, f = 1, 2, 3.$$

Typically, the Hamming distances computed for each filter are fused using sum rule to produce a final matching score.

$$D_{ijsum} = HD_{ij}^1 + HD_{ij}^2 + HD_{ij}^3.$$

The above described steps employed by a typical iris matcher are presented in the form of a flow chart in Figure 4.3.

### 4.3 Histogram of matching patterns

Based on the aforementioned discussion, three filter outputs are available at each pixel location in an iris image. Hence three filter matching results  $(r^1, r^2, r^3)$  are generated at every location when two IrisCode sets are matched. These three results at each location may be combined and represented as a single vector,  $R$ , which is referred to as **matching bit pattern** at every bit location. It can have values such as 000, 001, 010, ..., 111. Here, 000 at a specific location would mean that the pixel is matched by all filter scales; 100 would mean that although the pixel is mis-matched at filter 1, it is matched by filter 2 and filter 3. Similarly, 111 would indicate that the pixel is mis-matched at all filter scales.

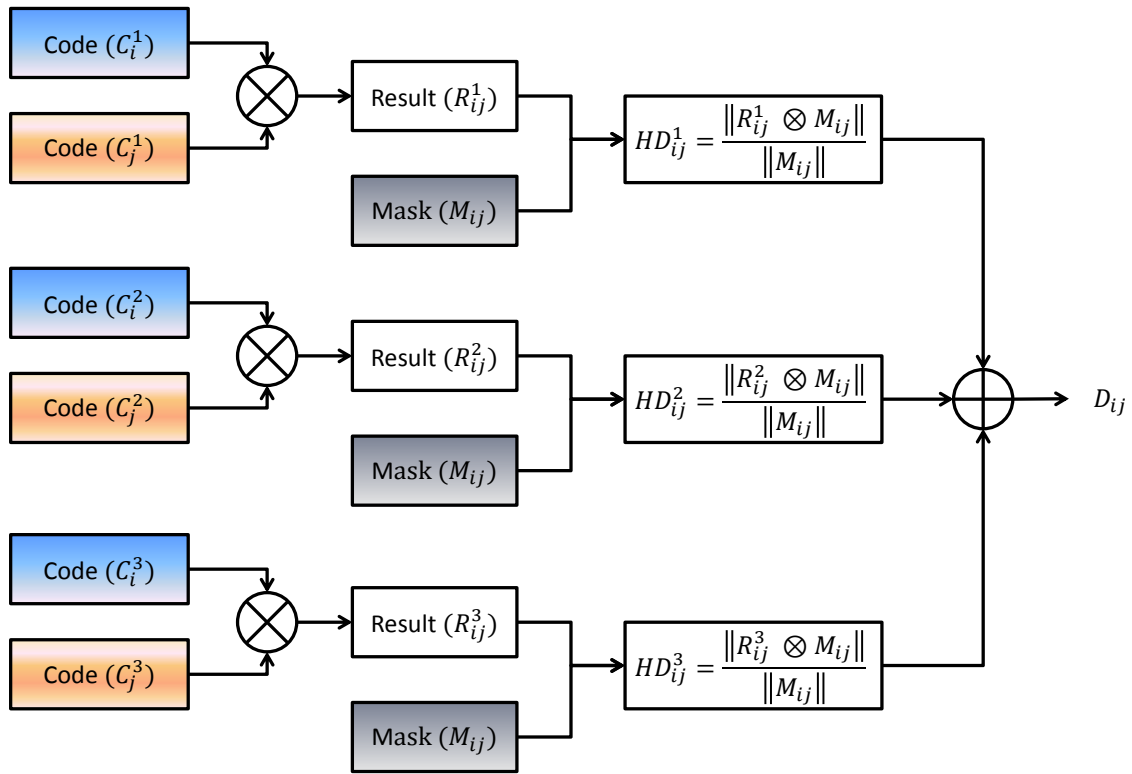


Figure 4.3 A typical iris matcher. Match scores are computed independently at each scale which are then fused at score level to result in a final distance score.

Figure 4.4 shows distribution of these matching patterns for one subject. The legend in the plots denotes the size of the pupil radius in pixels of the two images that are being matched. It is observed that the percentage of 000s (matched at all filters) decreases with increase in difference of pupil dilation ratios between the matched samples. Figure 4.5 shows distributions of multi-filter matching patterns for a few randomly selected inter-class (impostor) pairs in the dataset. It is observed that the distribution of these decisions is roughly equal and similar across the decision patterns.

In a traditional sum rule matcher, the instances of 000, 001, ..., 111 would have been merely summed up and divided by the total number of locations. This would mask some of the interesting properties observed in these patterns. Figure 4.6 shows the distribution of these matching results

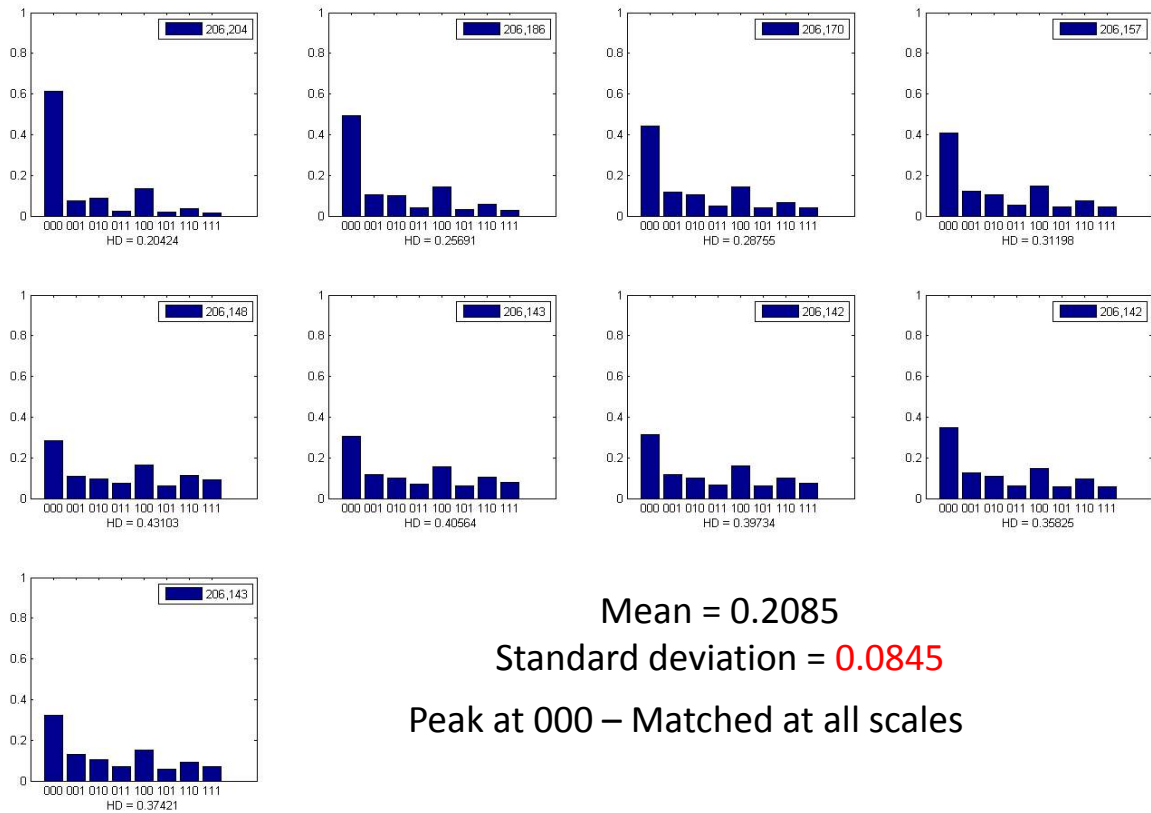


Figure 4.4 Distribution of multi-filter decisions for genuine matching cases for a single subject.

at three different filter scales for the genuine and impostor cases.

It is observed from Figure 4.6 that some matching patterns, such as 000, 011, 101, 110 and 111, are much more discriminative compared to others. Hence, these filter decisions could be selectively fused to provide better performance.

#### 4.4 Fusion

The idea behind the proposed method is to make a matching decision at *each pixel location* based on information at multiple scales. The distribution of decision patterns shown in the previous sections are exploited to come up with a better decision strategy. IrisCode bits generated from multiple filters are selectively matched to compute a final dissimilarity score. This is pictorially

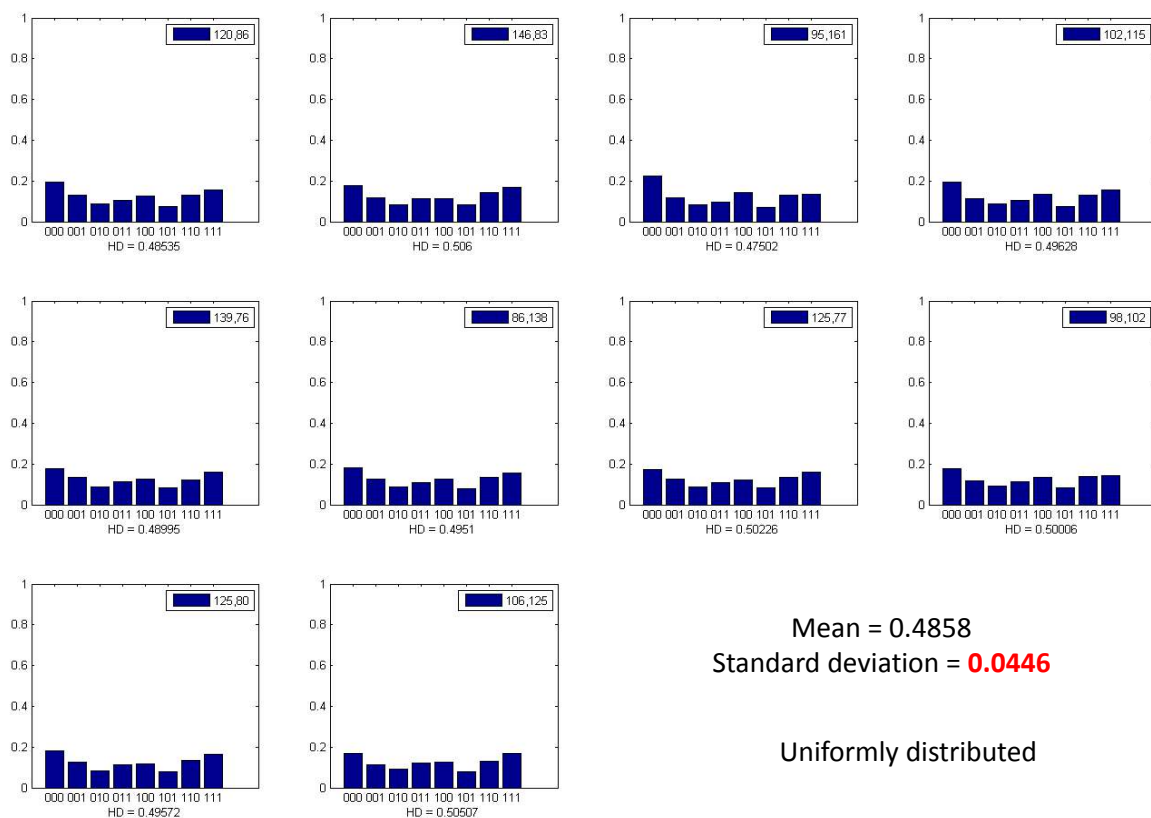


Figure 4.5 Distribution of multi-filter decisions for randomly selected impostor matching cases

depicted in Figure 4.7.

#### 4.4.1 Rule based Fusion

Multiple decision strategies can be developed to allow for strict or relaxed matching conditions. The proposed matching strategies are described below.

##### Method 1:

Two iris images ( $I_i, I_j$ ) are first matched using IrisCodes generated by filter 1 at each bit location,  $r^1 = (c_i^1, c_j^1)$ . If the images are not matched at filter 1, i.e.  $r^1 = 1$ , then the matching is extended to IrisCodes generated by larger filters 2 and 3. The bit location is deemed a match, if IrisCodes are at least matched by filters 2 and 3. This helps in handling *local defor-*

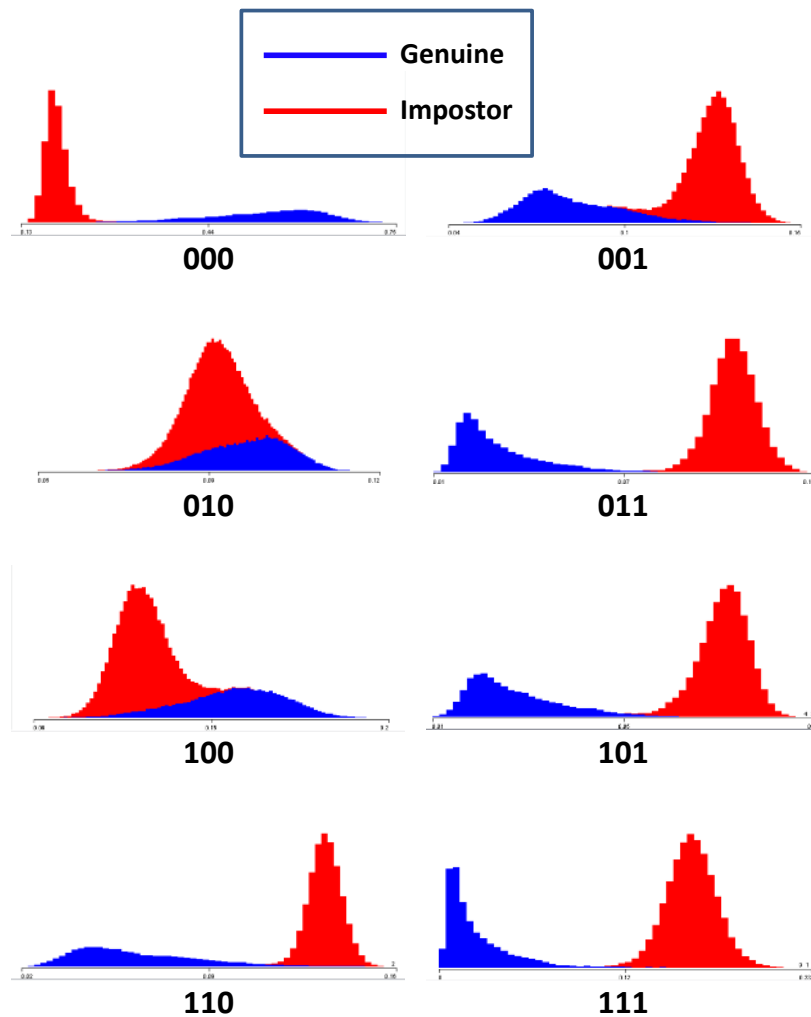


Figure 4.6 Comparison of distributions of possible multi-filter decisions for genuine and impostor matching cases

*mations* since match is established at a larger scale for those bits that would have otherwise mismatched at smaller scales.

**Method 2:**

This method relaxes the conditions for a match. If two IrisCodes are not matched at the lowest scale, an additional opportunity is provided at medium scale filter 2. In case IrisCodes are not matched at filter 2, then a final opportunity is afforded at larger filter 3. This method

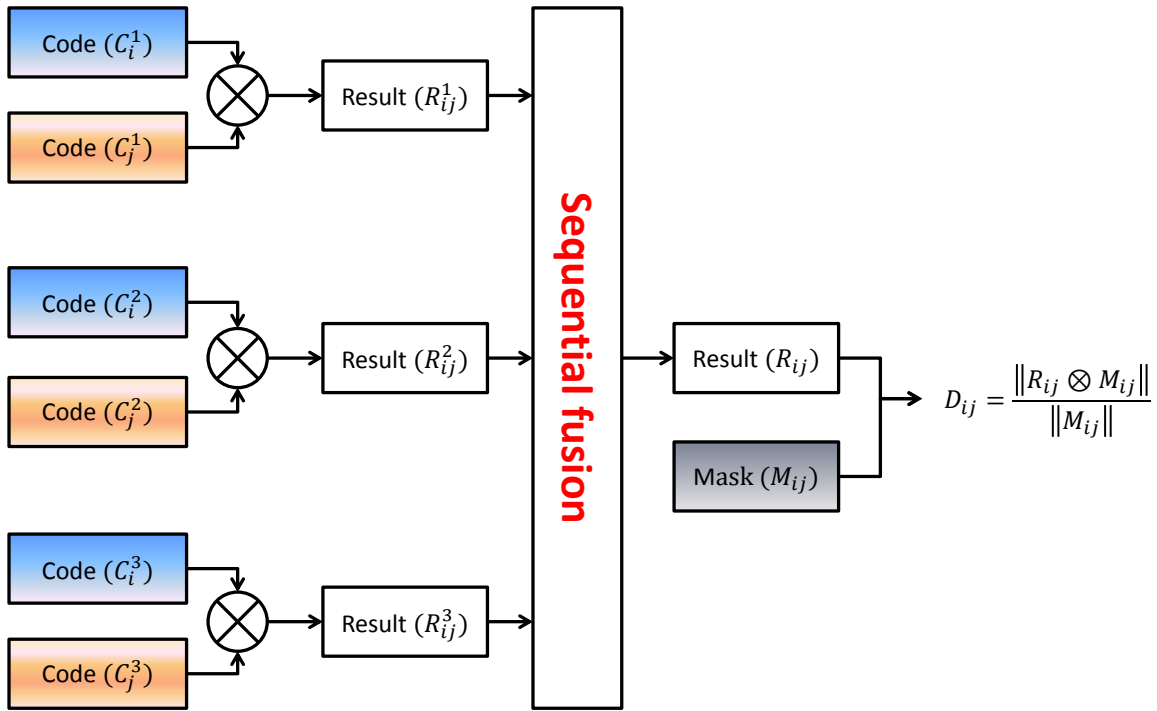


Figure 4.7 The proposed iris matcher sequentially combines the results at multiple scales and generates a single decision result.

allows for a positive match if the iris regions are matched at least in one of the scales.

### Method 3:

This method provides a stricter matching criterion compared to all the other methods by requiring the IrisCodes to match at filter 1 as well as either filter 2 or filter 3. This method *removes* the possibility of matching locally deformed regions. Only those regions that are matched at multiple scales are deemed a match.

The logical operations shown in Figures 4.8, 4.9 and 4.10 are used in the sequential fusion step in Figure 4.7 and can be implemented using a single Boolean expression. Corresponding truth tables are used to derive the Boolean expression that directly computes the final result based on the

Table 4.1 Logical operations used to combine the output of multiple IrisCodes.

Fusion	Logic
Sum rule	$R^1 + R^2 + R^3$
Method 1	$R^1 \& (R^2   (\sim R^2 \& R^3))$
Method 2	$R^1 \& R^2 \& R^3$
Method 3	$R^1   (\sim R^1 \& R^2 \& R^3)$

decisions at each scale. Hence, a single decision is made,  $r = 0$  (match) and  $r = 1$  (non-match), at each bit location in an IrisCode. The final decision is equivalent to applying a single complex filter on the normalized image. Let the final matching decision bits be presented in a matrix  $R$ . Hamming Distance between two IrisCode sets  $(C_i^1, C_i^2, C_i^3, M_i)$  and  $(C_j^1, C_j^2, C_j^3, M_j)$  is then given by

$$D_{ij} = \frac{\|r_{ij} \cap M_{ij}\|}{\|M_{ij}\|}.$$

Table 4.1 shows the logical operations for these three methods along with the simple sum rule fusion.

#### 4.4.2 Classifier based Fusion

As seen in the previous section, a histogram of matching patterns is being generated for every pair of images that are being matched. A linear SVM classifier was trained using histograms of matching patterns for genuine and impostor cases on a training dataset. Given a new pair of iris images, the trained classifier was used to predict if the new histogram of matching patterns pertains to the genuine or a impostor case. The obtained results were found to comparable to the Method 1 proposed in the previous section. However, further research on this topic will be necessary.

### 4.5 Experiments and Results

The proposed methods are tested on left eye images acquired at full illumination in the proprietary pupil dilation dataset. A total of 2218 images of left eyes from 52 subjects is used to test the proposed methods. The images are *automatically* segmented, normalized and encoded using the

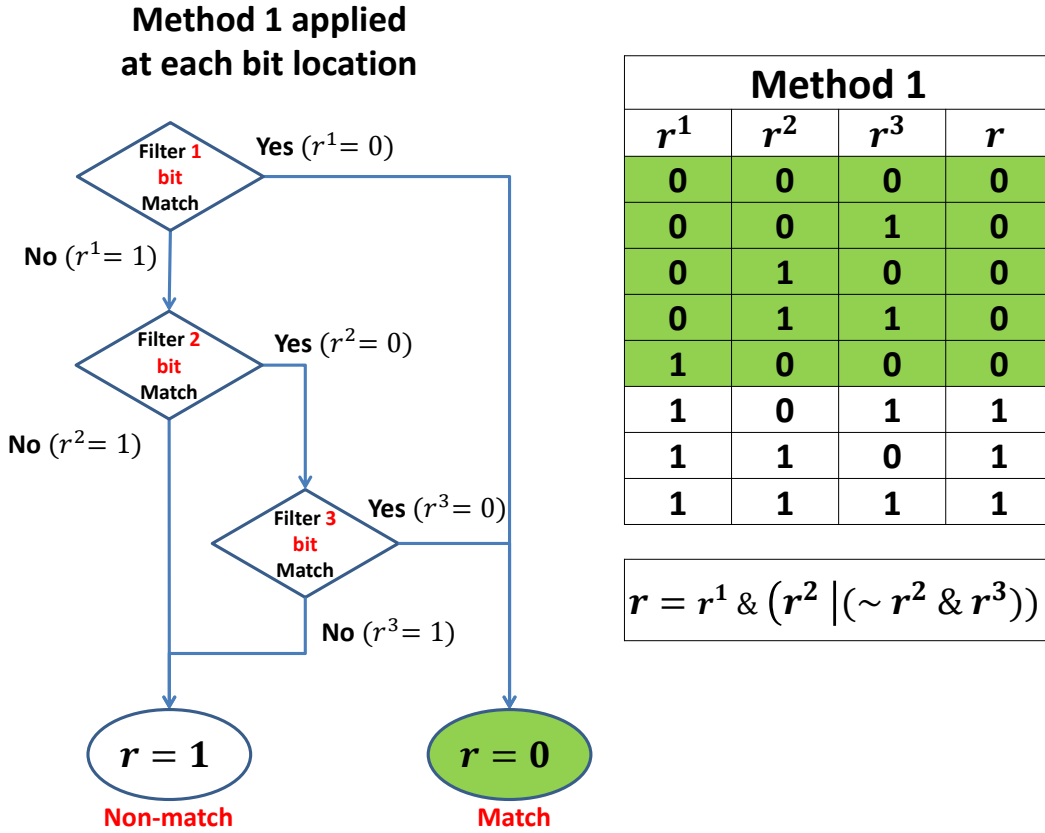


Figure 4.8 Flowchart depicting Method 1 and its corresponding truth table

OSIRIS\_v4.1 SDK. Semilog ROCs are presented to better observe the performance at low FARs. A total of 46,480 genuine scores and 1,696,504 impostor scores are generated. Figure 4.11 (a) shows ROCs for the full data. It is clearly seen that all the three methods clearly improve upon the traditional sum rule fusion method. However, generic matching using Masek’s 1-D encoded IrisCodes [4] is observed to provide better stand alone performance. Judicious parameter tuning using 2-D Gabor filter would probably yield better performance, in which case the proposed method is expected to further improve the performance. It can also be observed that fusing scores from Method 1 with match scores from Masek’s 1-D encoded IrisCode results in the overall best performance.

In order to observe the impact of the proposed methods on deformed iris patterns, scores from the traditional matching methods and proposed methods based on differences in pupil dilation

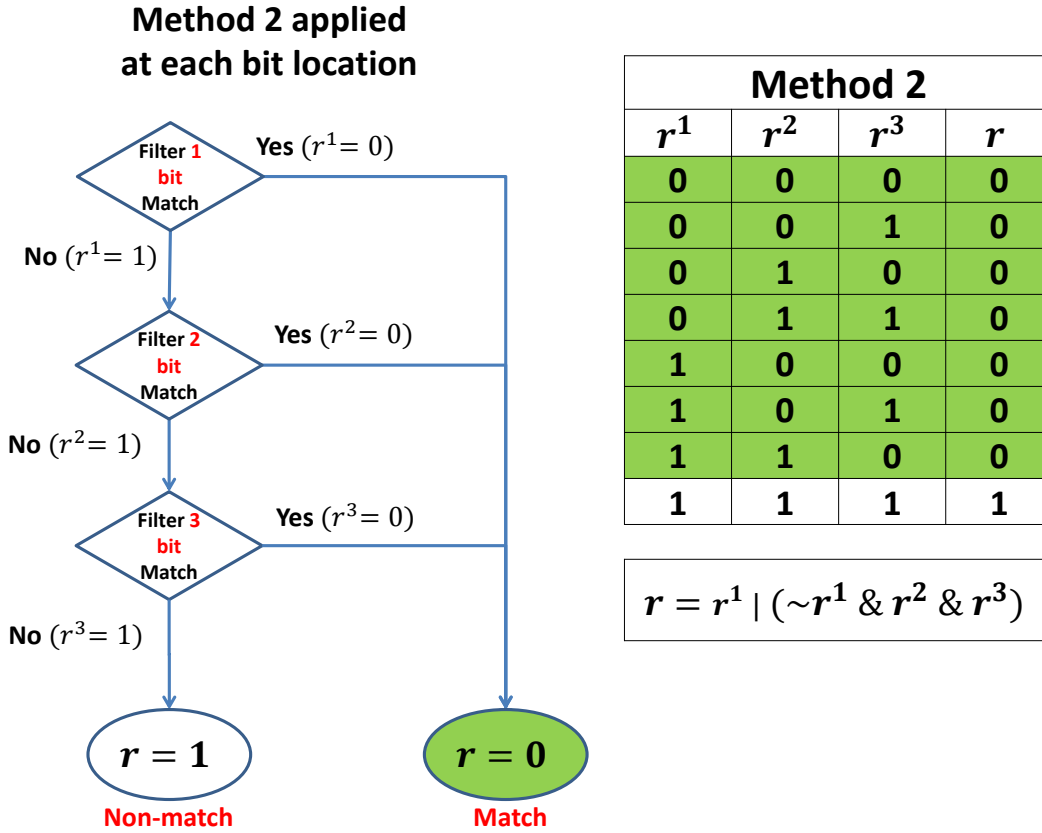


Figure 4.9 Flowchart depicting Method 2 and its corresponding truth table

ratio are examined. The genuine scores are divided into three dilation groups - small, medium and large - depending on the absolute value of the difference in pupil dilation ratio between the pair of images being matched. Impostor distributions are kept the same for the respective methods. These ROCs are shown in Figure 4.12. It is evident from the ROC plots in Figure 4.12 that the proposed methods have a larger impact when comparing highly deformed patterns than when comparing two images with almost the same pupil dilation values. Fusing best performing Method 1 with Masek 1-D method [4] results in the best overall performance when comparing images with larger differences in pupil sizes. Figure 4.13 shows the histogram distributions of genuine and impostor scores for Masek's method alone and after fusing the Masek's score with the match score from Method 1.

These matching methods are not just limited to handling deformation due to pupil dilation/constriction

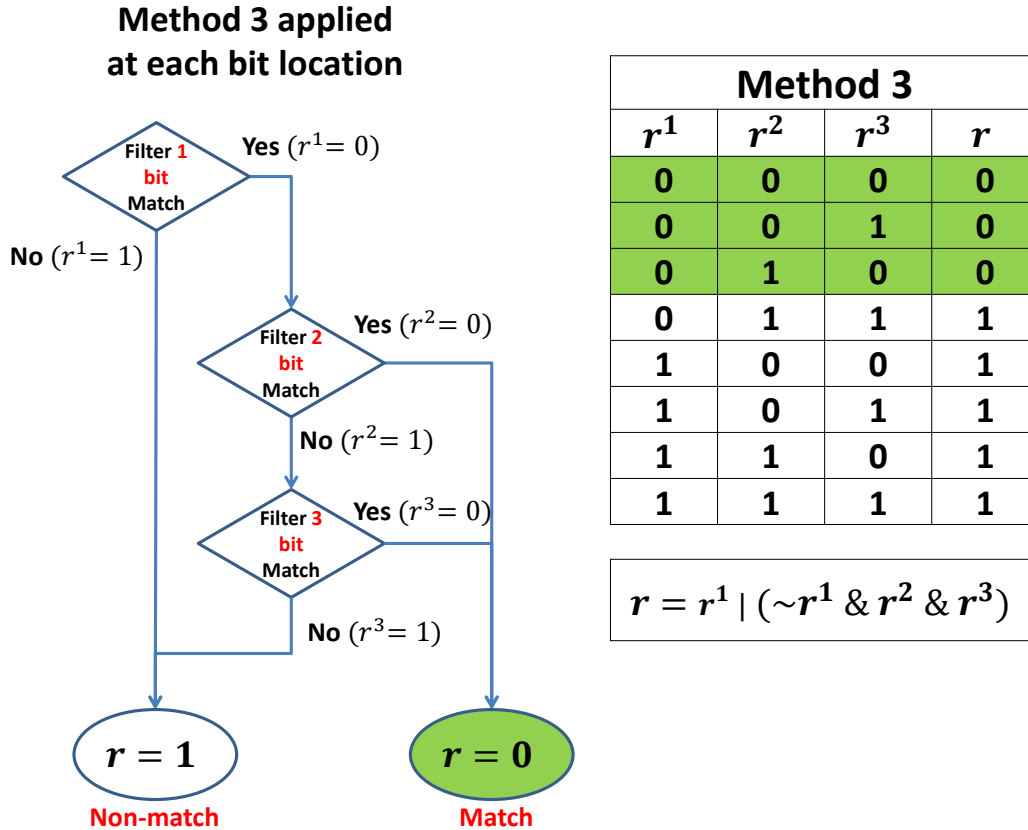


Figure 4.10 Flowchart depicting Method 3 and its corresponding truth table

alone, but can be used to handle non-ideal iris images. To validate the efficacy of these methods, experiments were conducted on the WVU non ideal [82] and QFire [83] datasets as well. The WVU non-ideal dataset has 1557 images from 241 subjects obtained under non-ideal conditions exhibiting the presence of blur, out of focus and occlusion. A total of 5277 genuine scores and 1206069 impostor scores are generated on the WVU dataset. QFire has 1304 left eye images from 90 subjects imaged at various acquisition distances. A total of 8847 genuine scores and 840709 impostor scores are generated on the QFire dataset. Figure 4.14 shows the result of applying the proposed matching methods on WVU and QFire datasets, and the improvement in performance is clearly observed.

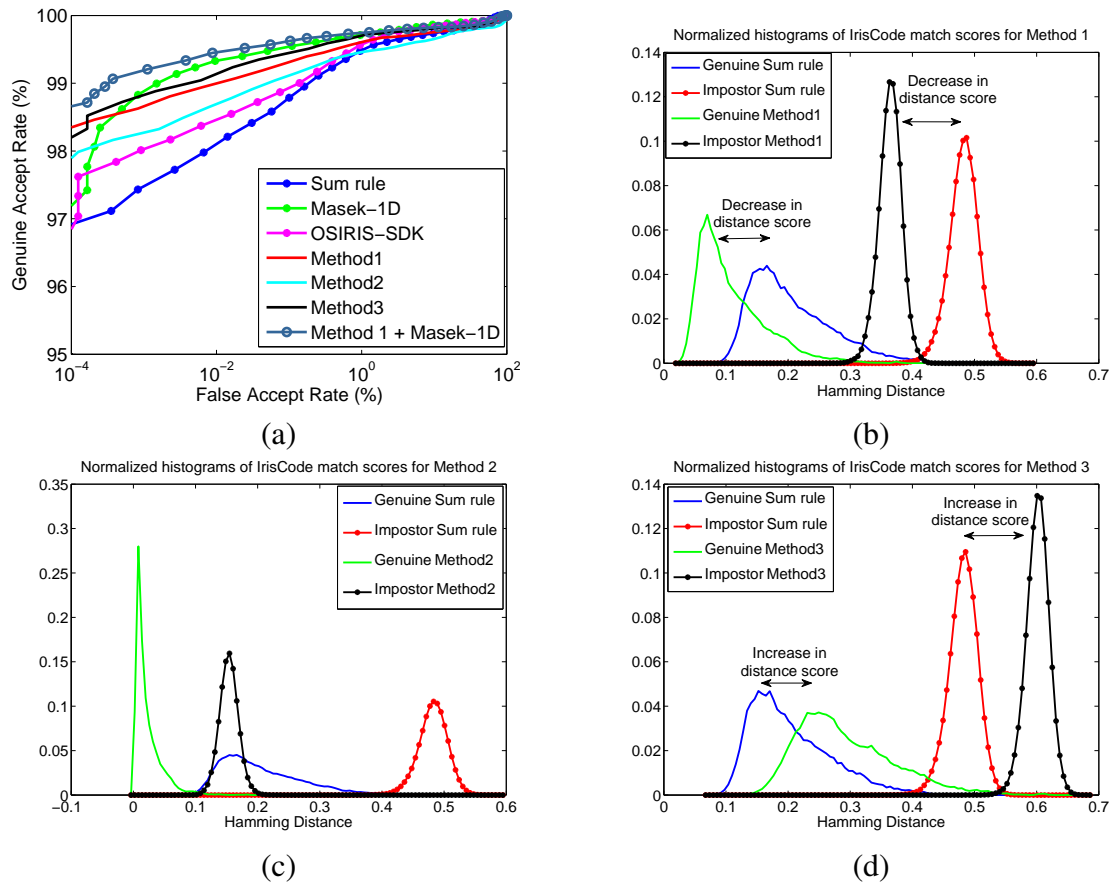


Figure 4.11 (a) ROCs for full data. The genuine and impostor score distributions are plotted for (b) Method 1, (c) Method 2 and (d) Method 3.

## 4.6 Examples

The proposed rule-based matching method is able to provide better verification performance over the traditional method. This implies that at a low operating FAR of, say, 0.0001% FAR a dilated probe image that would not have previously matched with a non-dilated image in the gallery would now be correctly identified using the new matching scheme. Examples of such pairs of images are shown in Figure 4.15. It is however possible that the improvement may not be apparent, or can result in a false mis-match when comparing genuine pair images with similar pupil size but large Hamming distance (due to occlusion/specular reflections).

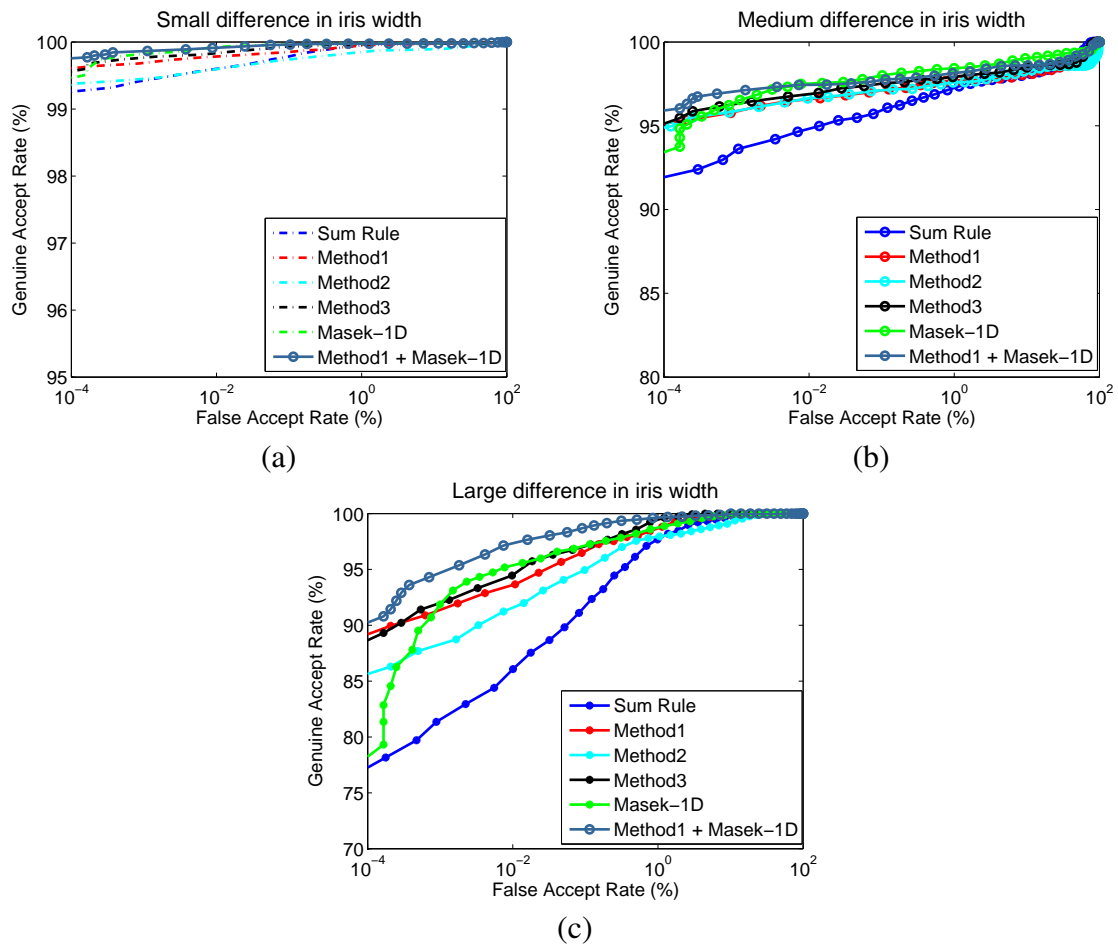


Figure 4.12 ROCs generated by using the genuine scores for pairs whose pupil dilation ratio differences are (a) small, (b) medium and (c) large. The impostor distributions are held the same across all the cases.

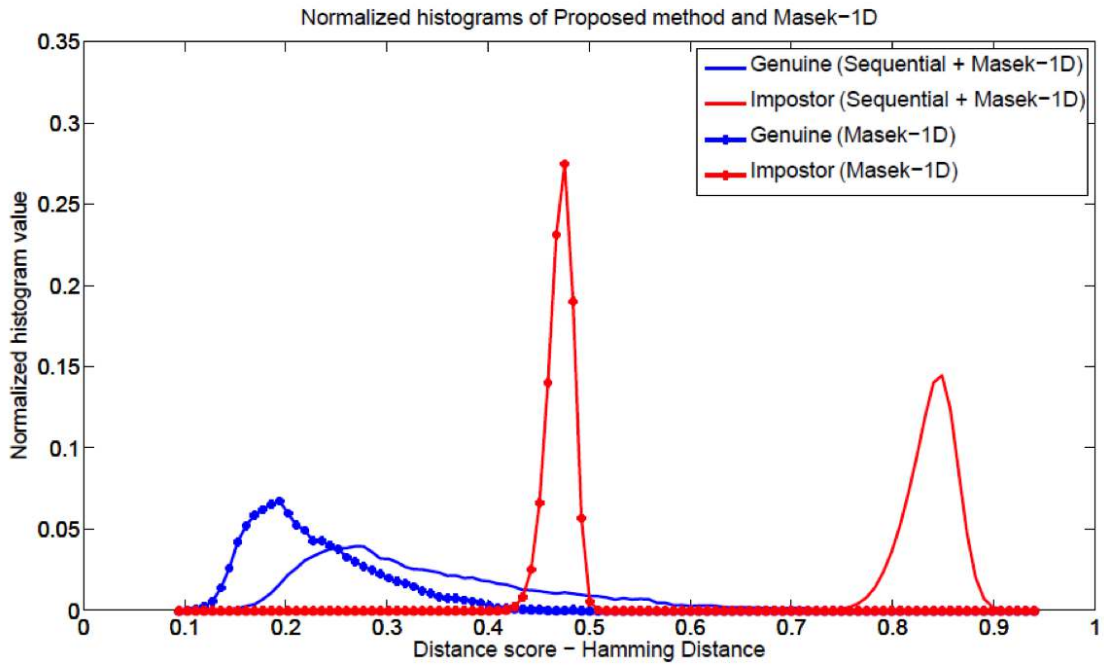


Figure 4.13 The histogram of genuine and impostor scores using Masek’s method and after fusion of match scores from Masek’s method and proposed Method 1.

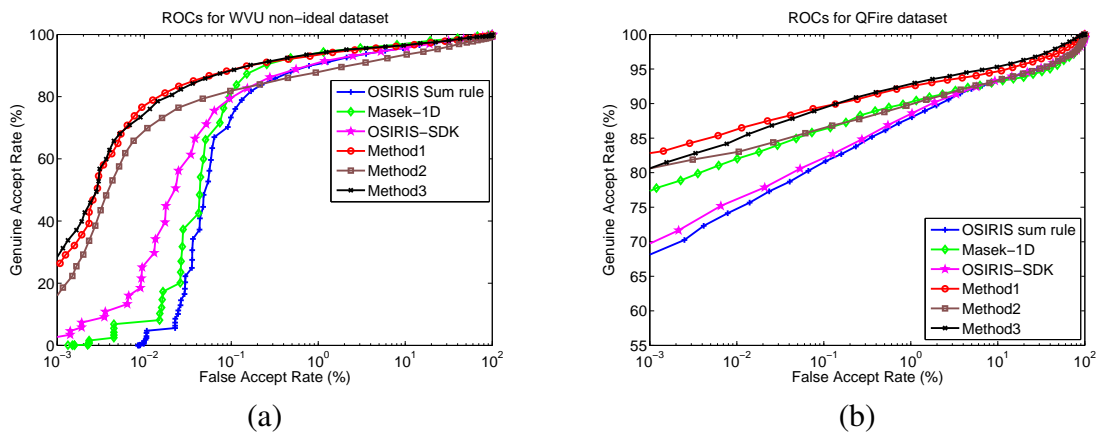


Figure 4.14 ROC curves for (a) WVU and (b) QFire datasets. The improvement in GAR is clearly evident at low FARs.

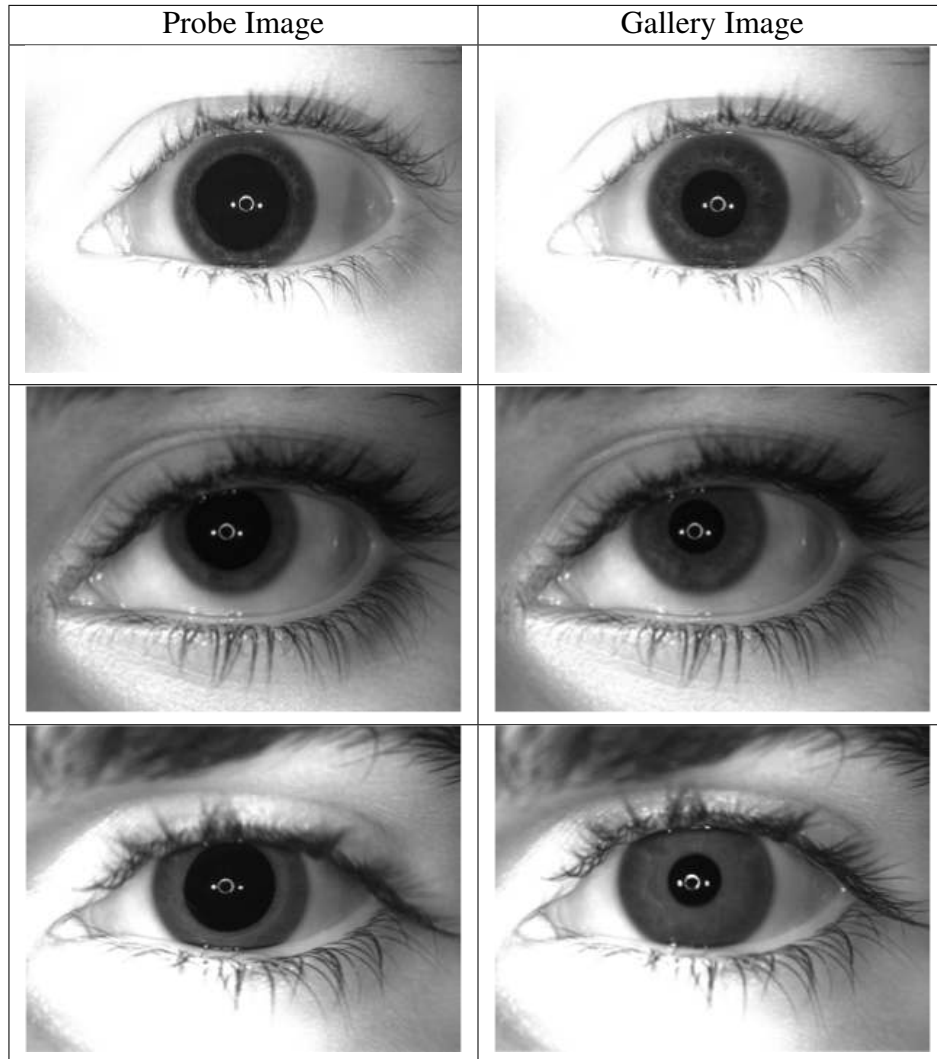


Figure 4.15 Genuine pairs of images that were correctly matched using the proposed method but were incorrectly rejected by the traditional matching method at 0.0001% FAR.

## CHAPTER 5

### SUMMARY

#### 5.1 Summary

A novel selective matching scheme based on IrisCodes obtained using multiscale filters is proposed. The three proposed methods integrate the decisions made at the bi (or pixel) level, thereby accounting for local deformations. The proposed approach is shown to significantly improve the matching accuracy when comparing images with large differences in pupil dilation ratio. It is also shown to improve the performance when non-ideal irides are compared where multiple factors including improper segmentation, off-gaze images could negatively influence matching accuracy. Future work will aim at exploring other matching strategies, which are based on a deeper understanding of the advantage of these methods.

The distribution of multi filter decision patterns could be used as a feature vector and a classifier could be trained to select the best decision strategy. In this work, filter sizes are increased along the angular direction; in future, we aim to explore other filter sets such as those varying increasing in the radial direction, or those radial and angular filters, etc. In addition, the possibility of designing new encoding schemes based on the results of this thesis will be explored. In particular, bit-level decision integration can allow for the generation of spatial statistics that can potentially provide deeper insights into the variation of the iris texture of an individual.

## **BIBLIOGRAPHY**

## BIBLIOGRAPHY

- [1] Helga Kolb, “Webvision,” <http://www.nextgenid.com/>.
- [2] Kebes at English Wikipedia, “Absorption spectrum of water,” [http://commons.wikimedia.org/wiki/File:Absorption\\_spectrum\\_of\\_liquid\\_water.png](http://commons.wikimedia.org/wiki/File:Absorption_spectrum_of_liquid_water.png).
- [3] Nikiforos Kollias, “The spectroscopy of human melanin pigmentation,” in *Journal of Investigative Dermatology*. BLACKWELL SCIENCE INC 238 MAIN ST, CAMBRIDGE, MA 02142, 1994, vol. 102, pp. 268–268.
- [4] L. Masek, “MATLAB source code for a Biometric Identification System Based on Iris Patterns,” *The School of Computer Science and Software Engineering, The University of Western Australia*, 2003.
- [5] Z. Wei, T. Tan, and Z. Sun, “Nonlinear iris deformation correction based on gaussian model,” *Advances in Biometrics*, pp. 780–789, 2007.
- [6] K. Hollingsworth, K.W. Bowyer, and P.J. Flynn, “Pupil dilation degrades iris biometric performance,” *Computer Vision and Image Understanding*, vol. 113, no. 1, pp. 150–157, 2009.
- [7] H. Rohen, “Der bau der regenbogenhaut beim menschen und einigen säugern,” *Gegenbaur Morphology Journal*, vol. 91, pp. 140, 1951.
- [8] H.J. Wyatt, “A ‘minimum-wear-and-tear’ meshwork for the iris,” *Vision Research*, vol. 40, no. 16, pp. 2167–2176, 2000.
- [9] X. Yuan and P. Shi, “A non-linear normalization model for iris recognition,” *Advances in Biometric Person Authentication*, pp. 135–141, 2005.
- [10] Ageev at Wikimedia Commons, “Image of human eye,” [http://commons.wikimedia.org/wiki/File:Ageev\\_iris.jpg](http://commons.wikimedia.org/wiki/File:Ageev_iris.jpg).
- [11] Anil K Jain, Karthik Nandakumar, and Arun Ross, “50 years of biometric research: Accomplishments, challenges, and opportunities,” *Pattern Recognition Letters*, 2016.
- [12] “ISO/IEC 2382-37:2012,” [http://www.iso.org/iso/home/store/catalogue\\_tc/catalogue\\_detail.htm?csnumber=55194](http://www.iso.org/iso/home/store/catalogue_tc/catalogue_detail.htm?csnumber=55194).
- [13] Dinei Florencio and Cormac Herley, “A large-scale study of web password habits,” in *Proceedings of the 16th international conference on World Wide Web*. ACM, 2007, pp. 657–666.
- [14] A.K. Jain, A. Ross, and S. Prabhakar, “An introduction to biometric recognition,” *IEEE Transactions on Circuits and Systems for Video Technology*, vol. 14, no. 1, pp. 4–20, 2004.
- [15] Brian DeCann and Arun Ross, ““has this person been encountered before?”: Modeling an anonymous identification system,” in *Computer Vision and Pattern Recognition Workshops (CVPRW)*. IEEE, 2012, pp. 89–96.

- [16] Nathan D Kalka, Jinyu Zuo, Natalia A Schmid, and Bojan Cukic, “Image quality assessment for iris biometric,” in *Defense and Security Symposium*. International Society for Optics and Photonics, 2006, pp. 62020D–62020D.
- [17] J. Daugman, “How iris recognition works,” *IEEE Transactions on Circuits and Systems for Video Technology*, vol. 14, no. 1, pp. 21–30, 2004.
- [18] Reza Derakhshani, Arun Ross, and Simona Crihalmeanu, “A new biometric modality based on conjunctival vasculature,” *Proc. of Artificial Neural Networks in Engineering (ANNIE)*, pp. 1–8, 2006.
- [19] Robert B Hill and Joel C Johnson, “Eye fundus optical scanner system and method,” July 2 1996, US Patent 5,532,771.
- [20] Pawel Kasprowski and Józef Ober, “Eye movements in biometrics,” in *Biometric Authentication*, pp. 248–258. Springer, 2004.
- [21] Corey D Holland and Oleg V Komogortsev, “Biometric verification via complex eye movements: The effects of environment and stimulus,” in *Biometrics: Theory, Applications and Systems (BTAS)*. IEEE, 2012, pp. 39–46.
- [22] Unsang Park, Arun Ross, and Anil K Jain, “Periocular biometrics in the visible spectrum: A feasibility study,” in *Biometrics: Theory, Applications, and Systems, 2009*. IEEE, 2009, pp. 1–6.
- [23] Richard A Sturm and Mats Larsson, “Genetics of human iris colour and patterns,” *Pigment cell & melanoma research*, vol. 22, no. 5, pp. 544–562, 2009.
- [24] Sunpreet S Arora, Mayank Vatsa, Richa Singh, and Anil Jain, “Iris recognition under alcohol influence: A preliminary study,” in *5th IAPR International Conference on Biometrics (ICB)*. IEEE, 2012, pp. 336–341.
- [25] V.F. Pamplona, M.M. Oliveira, and G.V.G. Baranoski, “Photorealistic models for pupil light reflex and iridal pattern deformation,” *ACM Transactions on Graphics (TOG)*, vol. 28, no. 4, pp. 106, 2009.
- [26] Hugo Proença, “On the feasibility of the visible wavelength, at-a-distance and on-the-move iris recognition,” in *Computational Intelligence in Biometrics: Theory, Algorithms, and Applications*. IEEE, 2009, pp. 9–15.
- [27] C. Boyce, A. Ross, M. Monaco, L. Hornak, and X. Li, “Multispectral iris analysis: A preliminary study,” in *CVPR workshop on Biometrics*, 2006.
- [28] A. Ross, R. Pasula, and L. Hornak, “Exploring multispectral Iris recognition beyond 900nm,” in *International Conference on Biometrics: Theory, Applications, and Systems (BTAS)*. IEEE, 2009, pp. 1–8.

- [29] Frederick W Wheeler, AG Amitha Perera, Gil Abramovich, Bing Yu, and Peter H Tu, “Stand-off iris recognition system,” in *Biometrics: Theory, Applications and Systems*. IEEE, 2008, pp. 1–7.
- [30] Wenbo Dong, Zhenan Sun, and Tieniu Tan, “A design of iris recognition system at a distance,” in *Chinese Conference on Pattern Recognition*. IEEE, 2009, pp. 1–5.
- [31] SRI international, “Weblink,” <http://www.sri.com/engage/products-solutions/iom-passport-portal-system>.
- [32] SRI international, “Weblink,” <http://www.sri.com/engage/products-solutions/iom-pass-thru-drive-up-iris-recognition-system>.
- [33] Vishnu Naresh Boddeti and BVK Vijaya Kumar, “Extended-depth-of-field iris recognition using unrestored wavefront-coded imagery,” *IEEE Transactions on Systems, Man and Cybernetics, Part A: Systems and Humans*, vol. 40, no. 3, pp. 495–508, 2010.
- [34] Sriram P Tankasala, Vikas Gottemukkula, Sashi Kanth Saripalle, Venkata Goutam Nalamati, Reza Derakhshani, Raghunandan Pasula, and Arun Ross, “A video-based hyper-focal imaging method for iris recognition in the visible spectrum,” in *IEEE Conference on Technologies for Homeland Security (HST)*, 2012, pp. 214–219.
- [35] Richard P Wildes, “Iris recognition: an emerging biometric technology,” *Proceedings of the IEEE*, vol. 85, no. 9, pp. 1348–1363, 1997.
- [36] L. Ma, Y. Wang, and T. Tan, “Iris recognition using circular symmetric filters,” in *Proceedings of the 16th International Conference on Pattern Recognition (ICPR)*, 2002, vol. 2, pp. 414–417.
- [37] Jinyu Zuo and Natalia A Schmid, “On a methodology for robust segmentation of nonideal iris images,” *IEEE Transactions on Systems, Man, and Cybernetics*, vol. 40, no. 3, pp. 703–718, 2010.
- [38] A. Ross and S. Shah, “Segmenting non-ideal irises using geodesic active contours,” in *Biometrics Symposium: Special Session on Research at the Biometric Consortium Conference*, 2006, pp. 1–6.
- [39] Kaushik Roy, Prabir Bhattacharya, and Ching Y Suen, “Unideal iris segmentation using region-based active contour model,” in *Image Analysis and Recognition*, pp. 256–265. Springer, 2010.
- [40] Mayank Vatsa, Richa Singh, and Afzel Noore, “Improving iris recognition performance using segmentation, quality enhancement, match score fusion, and indexing,” *IEEE Transactions on Systems, Man, and Cybernetics, Part B: Cybernetics*, vol. 38, no. 4, pp. 1021–1035, 2008.
- [41] Randy P Broussard, Lauren R Kennell, David L Soldan, and Robert W Ives, “Using artificial neural networks and feature saliency techniques for improved iris segmentation,” in *Neural Networks, 2007. IJCNN 2007. International Joint Conference on*. IEEE, 2007, pp. 1283–1288.

- [42] Zhaofeng He, Tieniu Tan, Zhenan Sun, and Xianchao Qiu, "Toward accurate and fast iris segmentation for iris biometrics," *IEEE Transactions on Pattern Analysis and Machine Intelligence*, vol. 31, no. 9, pp. 1670–1684, 2009.
- [43] Ruihui Zhu, Jinfeng Yang, and Renbiao Wu, "Iris recognition based on local feature point matching," in *International Symposium on Communications and Information Technologies*. IEEE, 2006, pp. 451–454.
- [44] Fernando Alonso-Fernandez, Pedro Tome-Gonzalez, Virginia Ruiz-Albacete, and Javier Ortega-Garcia, "Iris recognition based on sift features," in *International Conference on Biometrics, Identity and Security (BIDS)*. IEEE, 2009, pp. 1–8.
- [45] Wageeh W Boles and Boualem Boashash, "A human identification technique using images of the iris and wavelet transform," *IEEE transactions on signal processing*, vol. 46, no. 4, pp. 1185–1188, 1998.
- [46] Chia-Te Chou, Sheng-Wen Shih, Wen-Shiung Chen, and Victor W Cheng, "Iris recognition with multi-scale edge-type matching," in *18th International Conference on Pattern Recognition*. IEEE, 2006, vol. 4, pp. 545–548.
- [47] D de Martin-Roche, Carmen Sanchez-Avila, and Raul Sanchez-Reillo, "Iris recognition for biometric identification using dyadic wavelet transform zero-crossing," in *35th International Carnahan Conference on Security Technology*. IEEE, 2001, pp. 272–277.
- [48] Vivekanand Dorairaj, Natalia A Schmid, and Gamal Fahmy, "Performance evaluation of iris-based recognition system implementing pca and ica encoding techniques," in *Defense and Security*. International Society for Optics and Photonics, 2005, pp. 51–58.
- [49] Ya-Ping Huang, Si-Wei Luo, and En-Yi Chen, "An efficient iris recognition system," in *International Conference on Machine Learning and Cybernetics*. IEEE, 2002, vol. 1, pp. 450–454.
- [50] Li Ma, Tieniu Tan, Yunhong Wang, and Dexin Zhang, "Personal identification based on iris texture analysis," *IEEE Transactions on Pattern Analysis and Machine Intelligence*, vol. 25, no. 12, pp. 1519–1533, 2003.
- [51] Wen-Shiung Chen, Ren-Hung Huang, and Lili Hsieh, "Iris recognition using 3d co-occurrence matrix," in *Advances in Biometrics*, pp. 1122–1131. Springer, 2009.
- [52] Melvin Ember, *Encyclopedia of Sex and Gender: Men and Women in the World's Cultures Topics and Cultures AK-Volume 1; Cultures LZ*, vol. 2, Springer, 2003.
- [53] K.W. Bowyer, K. Hollingsworth, and P.J. Flynn, "Image understanding for iris biometrics: A survey," *Computer Vision and Image Understanding*, vol. 110, no. 2, pp. 281–307, 2008.
- [54] Kevin W Bowyer, Sarah E Baker, Amanda Hentz, Karen Hollingsworth, Tanya Peters, and Patrick J Flynn, "Factors that degrade the match distribution in iris biometrics," *Identity in the Information Society*, vol. 2, no. 3, pp. 327–343, 2009.

- [55] Registered Traveler Interoperability Consortium (RTIC), “Technical interoperability specification for the Registered Traveler Program (Version 1.0–Final),” Online, 2006.
- [56] Soumyadip Rakshit and Donald M Monro, “An evaluation of image sampling and compression for human iris recognition,” *IEEE Transactions on Information Forensics and Security*, vol. 2, no. 3, pp. 605–612, 2007.
- [57] John Daugman and Cathryn Downing, “Effect of severe image compression on iris recognition performance,” *IEEE Transactions on Information Forensics and Security*, vol. 3, no. 1, pp. 52–61, 2008.
- [58] Ishan Nigam, Mayank Vatsa, and Richa Singh, “Ocular biometrics: A survey of modalities and fusion approaches,” *Information Fusion*, vol. 26, pp. 1–35, 2015.
- [59] George McConnon, Farzin Deravi, Sanaul Hoque, Konstantinos Sirlantzis, and Gareth Howells, “Impact of common ophthalmic disorders on iris segmentation,” in *5th IAPR International Conference on Biometrics (ICB)*. IEEE, 2012, pp. 277–282.
- [60] Massimo Tistarelli and Mark S Nixon, *Advances in Biometrics: Third International Conferences, ICB 2009, Alghero, Italy, June 2-5, 2009, Proceedings*, vol. 5558, Springer, 2009.
- [61] Désirée White and Montserrat Rabago-Smith, “Genotype–phenotype associations and human eye color,” *Journal of human genetics*, vol. 56, no. 1, pp. 5–7, 2011.
- [62] Samuel P Fenker and Kevin W Bowyer, “Experimental evidence of a template aging effect in iris biometrics,” in *Workshop on Applications of Computer Vision (WACV)*. IEEE, 2011, pp. 232–239.
- [63] Irene E Loewenfeld and Otto Lowenstein, *The pupil: anatomy, physiology, and clinical applications*, vol. 2, Wiley-Blackwell, 1993.
- [64] G. Francois, P. Gautron, G. Breton, K. Bouatouch, et al., “Anatomically accurate modeling and rendering of the human eye,” 2007.
- [65] G. Francois, S. Pattanaik, K. Bouatouch, and G. Breton, “Subsurface texture mapping,” *SIGGRAPH*, 2006.
- [66] Antwan D Clark, Scott A Kulp, Isom H Herron, and AA Ross, “A theoretical model for describing iris dynamics,” in *Handbook of Iris Recognition*, pp. 129–150. Springer, 2013.
- [67] A.N. Palazotto and S.T. Dennis, *Nonlinear analysis of shell structures*, AIAA Education Services, 1992.
- [68] W.F. Carroll, *A Primer for Finite Elements in Elastic Structures*, John Wiley & Sons, Inc, 1999.
- [69] RS Gejji, AD Clark, S Crihalmeanu, and AA Rossy, “Understanding the subject-specific effects of pupil dilation on iris recognition in the nir spectrum,” in *IEEE International Symposium on Technologies for Homeland Security (HST)*. IEEE, 2015, pp. 1–6.

- [70] AD Clark, RS Gejji, AD Ridley, and AA Ross, “The states of dilation in iris recognition (a preliminary study),” in *IEEE International Symposium on Technologies for Homeland Security (HST)*. IEEE, 2015, pp. 1–5.
- [71] D. Terzopoulos and D. Metaxas, “Dynamic 3d models with local and global deformations: Deformable superquadrics,” in *Transactions on Pattern Analysis and Machine Intelligence*. IEEE, 1990, vol. 13.
- [72] M. Mooney, “A theory of large elastic deformation,” *Journal of Applied Physics*, vol. 11, no. 9, pp. 582–592, 1940.
- [73] F.L. Bookstein, “Principal warps: Thin-plate splines and the decomposition of deformations,” *IEEE Transactions on Pattern Analysis and Machine Intelligence*, vol. 11, no. 6, pp. 567–585, 1989.
- [74] Jason Thornton, Marios Savvides, and V Kumar, “A bayesian approach to deformed pattern matching of iris images,” *IEEE Transactions on Pattern Analysis and Machine Intelligence*, vol. 29, no. 4, pp. 596–606, 2007.
- [75] Inmaculada Tomeo-Reyes, Arun Ross, Antwan D Clark, and Vinod Chandran, “A biomechanical approach to iris normalization,” in *International Conference on Biometrics (ICB)*. IEEE, 2015, pp. 9–16.
- [76] L Dhir, NE Habib, DM Monro, and S Rakshit, “Effect of cataract surgery and pupil dilation on iris pattern recognition for personal authentication,” *Eye*, vol. 24, no. 6, pp. 1006–1010, 2009.
- [77] Orang Seyeddain, Hannes Kraker, Andreas Redlberger, Alois K Dexe, Guenther Grabner, and Martin Emesz, “Reliability of automatic biometric iris recognition after phacoemulsification or drug-induced pupil dilation,” *European journal of ophthalmology*, vol. 24, no. 1, pp. 58–62, 2013.
- [78] Karen P Hollingsworth, Kevin W Bowyer, and Patrick J Flynn, “The best bits in an iris code,” *Transactions on Pattern Analysis and Machine Intelligence*, vol. 31, no. 6, pp. 964–973, 2009.
- [79] Christian Rathgeb, Andreas Uhl, and Peter Wild, “On combining selective best bits of iris-codes,” in *Biometrics and ID Management*, pp. 227–237. Springer, 2011.
- [80] Christian Rathgeb, Andreas Uhl, and Peter Wild, “Shifting score fusion: On exploiting shifting variation in iris recognition,” in *Proceedings of the 2011 ACM Symposium on Applied Computing*. ACM, 2011, pp. 3–7.
- [81] James E Gentile, Nalini Ratha, and Jonathan Connell, “An efficient, two-stage iris recognition system,” in *Biometrics: Theory, Applications, and Systems*. IEEE, 2009, pp. 1–5.
- [82] S. Crihalmeanu, Arun Ross, Stephanie Schuckers, and L. Hornak, “A protocol for multibiometric data acquisition, storage and dissemination,” *WVU, Lane Dept. of Computer Science and Electrical Eng., Morgantown, WV, Technical Report*, 2007.

- [83] S. Schuckers, P. Lopez, P. Johnson, N. Sazonova, F. Hua, R. Lazarick, C. Miles, E. Talbassi, E. Sazonov, A. Ross, and L. Hornak, “Quality–face / iris research ensemble (q-fire) dataset overview,” *Clarkson University, Dept of Electrical and Computer Engineering, Technical Report*, 2010.